Excited-State Contributions to Ground-State Properties of Mixed-Valence Dimers: Spectral and Electronic-Structural Studies of $[Fe_2(OH)_3(tmtacn)_2]^{2+}$ Related to the $[Fe_2S_2]^+$ Active Sites of Plant-Type Ferredoxins

Daniel R. Gamelin,[†] Emile L. Bominaar,[‡] Martin L. Kirk,[†] Karl Wieghardt,[§] and Edward I. Solomon*,[†]

Contribution from the Department of Chemistry, Stanford University, Stanford, California 94305, Department of Chemistry, Carnegie Mellon University, Pittsburgh, Pennsylvania 15213, and Max-Planck-Institut für Strahlenchemie, Stiftstrasse 34-36, D-45470 Mülheim an der Ruhr, Germany

Received October 31, 1995. Revised Manuscript Received April 11, 1996[⊗]

Abstract: The electronic transitions of the $S = 9/2$ class III mixed-valence dimer $[Fe_2(OH)_3(tmtacn)_2]^{2+}$ are assigned using absorption, magnetic circular dichroism (MCD), and resonance Raman (RR) spectroscopies. This set of excited-state assignments allows the relative contributions of metal−metal and metal−ligand interactions to the D_{3h} molecular-orbital energy splittings to be estimated. From this analysis the pathway for valence delocalization in this dimer is determined to involve a significant direct Fe···Fe σ-bonding interaction. The spectroscopic analysis is supported by electronic-structure calculations, which predict a spectrum similar to that observed and provide descriptions of the dimer's molecular orbitals. These results are further supported by the observation of a significant increase in the Fe···Fe internuclear separation with $\sigma-\sigma^*$ excitation, determined by vibronic analysis of the $\sigma-\sigma^*$ absorption band shape and associated RR excitation profiles. Combined, these results provide a measure of the geometry dependence of the double-exchange electron-transfer parameter, B, that dominates the ground-state magnetic properties of this dimer. The excited-state assignments also identify the superexchange pathways active in this dimer and provide a spectroscopic measure of the ground-state Heisenberg exchange-coupling constant, yielding $-23 < J < +2$ cm^{-1}. The fact that J is small is confirmed by variable-temperature magnetic-susceptibility experiments, which provide an upper limit of $\sim$70 cm^{-1} for the magnitude of antiferromagnetic coupling in this dimer. The contributions of B, J, and vibronic coupling to the valence-delocalized $S = 9/2$ ground state of $[Fe_2(OH)_3(tmtacn)_2]^{2+}$ are related to the analogous properties of mixed-valence iron−sulfur and other non-heme iron dimers. From this comparison it is concluded that significant direct Fe−Fe electronic coupling also occurs in $[Fe_2S_2]^+$ dimers, but the combination of an order-of-magnitude increase in Heisenberg exchange coupling relative to that of $[Fe_2(OH)_3(tmtacn)_2]^{2+}$ and the greater influence of vibronic-coupling terms in $S = 1/2$ *vs* $S = 9/2$ states outweighs this electronic coupling and leads to the valence-trapped antiferromagnetically-coupled ground state observed in $[Fe_2S_2]^+$ dimers. The difference in Heisenberg exchange between the $[Fe_2(OH)_3(tmtacn)_2]^{2+}$ and $[Fe_2S_2]^+$ dimers is related to specific differences in the superexchange pathways and covalencies of metal−bridge interactions.

Introduction

Mixed-valence transition-metal clusters have played an important role in the development of fundamental concepts in coordination chemistry related to cluster interactions and electron transfer (ET).[1−3] The study of these systems is often motivated by the observation of unusual spectral or magnetic features and the possibility of using these features as probes of electronic delocalization. Mixed−valence clusters are also found in a variety of redox and ET metalloenzymes of iron (e.g., iron−sulfur clusters, hemerythrin, uterroferrin),[4−6] copper (e.g., hemocyanin, tyrosinase, the Cu_A site in cytochrome oxidases and nitrous oxide reductase),[7−9] and manganese (e.g., the Mn water-oxidation catalyst of photosystem II).[10] The specific contributions of mixed valency to the biological reactivities of these systems are of fundamental interest in the field of mechanistic bioinorganic chemistry.

Mixed-valence systems are traditionally classified by the extent of delocalization of the "extra" electron, which ranges from complete localization (class I) to complete delocalization (class III) depending on the efficiency of electronic coupling between the ions.[11] The extent of valence delocalization in turn determines many of the observable spectral properties, such as

---

[†] Stanford University.

[‡] Carnegie Mellon University.

[§] Max-Planck-Institut für Strahlenchemie.

[⊗] Abstract published in *Advance ACS Abstracts,* August 1, 1996.

(1) *Mixed Valency Systems: Applications in Chemistry, Physics, and Biology*; Prassides, K., Ed.; Kluwer Academic Publishers: Dordrecht, The Netherlands, 1991.

(2) *Mechanistic Aspects of Inorganic Reactions*; Rorabacher, D. B., Endicott, J. F., Eds.; ACS Symposium Series; American Chemical Society: Washington, DC, 1982; Vol. 198.

(3) *Mixed-Valence Compounds*; Brown, D. B., Ed.; Reidel: Dordrecht, The Netherlands, 1980.

(4) *Iron-Sulfur Proteins*; Cammack, R., Ed.; Adv. Inorg. Chem., Vol. 38; Academic Press, Inc.: San Diego, 1992.

(5) *Iron-Sulfur Proteins*; Spiro, T. G., Ed.; Wiley and Sons: New York, 1982.

(6) Que, L., Jr.; True, A. E. *Prog. Inorg. Chem.* **1990**, *38*, 97−200.

(7) Solomon, E. I. In *Metal Clusters in Proteins*; Que, L., Jr., Ed.; ACS Symposium Series; American Chemical Society: Washington, DC, 1988; Vol. 372, pp 116−150.

(8) *Bioinorganic Chemistry of Copper*; Karlin, K. D., Tyeklár, Z., Eds.; Chapman & Hall Inc.: New York, 1993.

(9) Ramirez, B. E.; Malmström, B. G.; Winkler, J. R.; Gray, H. B. *Proc. Natl. Acad. Sci. U.S.A.* **1995**, *92*, 11949−11951.

(10) *Manganese Redox Enzymes*; Pecoraro, V. L., Ed.; VCH Publishers: New York, 1992.

S0002-7863(95)03663-8 CCC: $12.00

absorption, EPR, and Mössbauer features. In cases involving coupling of transition metals having more than one unpaired spin, an additional effect of valence delocalization may be observed in the magnetic properties of the dimer: As electronic coupling is increased these dimers may show a propensity to couple ferromagnetically, attributable to a spin-dependent electron-delocalization phenomenon referred to as double exchange.[12−16]

Exchange interactions in mixed-valence dimers with multiple unpaired electrons differ from those of their homovalent analogs in the existence of an additional "double-exchange" resonance coupling interaction. Resonance delocalization in such cases splits the Heisenberg spin states with the extra electron on either half of the dimer into symmetric ($E^{s} = \pm B(S + 1/2)$) and antisymmetric ($E^{a} = \mp B(S + 1/2)$) delocalized wavefunctions, where B is the absolute-value double-exchange parameter related to inter-ion electron transfer. The resonance-delocalization process entails spin-allowed electron transfer between ions and retains maximum spin-polarization stabilization when the unpaired electrons on each ion are aligned in a net ferromagnetic configuration. Delocalization in such cases therefore introduces a ferromagnetic spin-coupling term to the molecular spin Hamiltonian that competes with Heisenberg interactions ($H = -2JS_1 \cdot S_2$) in determining the relative energies of molecular spin states. The combination of these yields spin-ladder energetics given by $E^{s,a}(S) = -JS(S + 1) \pm B(S + 1/2)$. The resulting splitting between symmetric and antisymmetric spin components gives rise to a spin- and electric-dipole-allowed electronic transition (e.g., the symmetric → antisymmetric excitation), which in favorable cases can be used to evaluate the magnitude of B using the relationship $\Delta E^{s,a} = 2B(S + 1/2)$.

The majority of the mixed-valence sites in biology mentioned above are localized, including $[Fe_2S_2]^+$ dimers, but spectroscopic studies have demonstrated that mixed-valence $[Fe_2S_2]^+$ pairs found in tri- and tetranuclear iron−sulfur clusters of ferredoxins, as well as the dimeric Cu_A sites found in cytochrome *c* oxidases and nitrous oxide reductases, show properties of valence delocalization. In particular, magnetic-susceptibility and Mössbauer ground-state results on tri- and tetranuclear iron−sulfur clusters in proteins and small-molecule analogs have been interpreted as resulting from pairwise delocalization of $[Fe_2S_2]^+$ subunits to give ferromagnetically-coupled $S = 9/2$ pairs, which further couple antiferromagnetically within the cluster to yield reduced cluster magnetism. Theoretical studies of the relative contributions of J and B in iron−sulfur clusters[15,17−19] suggest that a sensitive balance among J, B, and vibronic trapping energies is responsible for determining the cluster spin topology. Although a great deal is known about the important contributions of excited states to ground-state magnetism in Heisenberg exchange-coupled dimers,[20−22] few experimental data exist that address excited-state contributions to the ground-state magnetic properties of mixed-valence dimers in which double exchange plays a significant role. The mixed-valence dimer $[Fe_2(OH)_3(tmtacn)_2]^{2+}$ is ideally suited for such studies due to its class III valence delocalization and strong stabilization of the ferromagnetic ground-state.

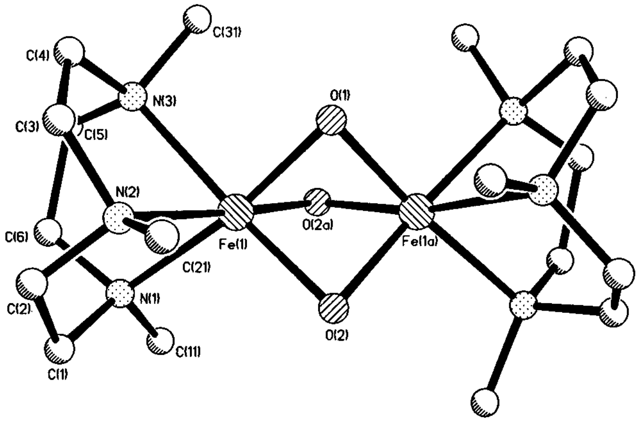

Figure 1. Depiction of the structure of $[Fe_2(OH)_3(tmtacn)_2]^{2+}$, obtained from 198 K X-ray diffraction data. The idealized D_{3h} structural parameters used in the text are Fe···Fe (2.509 Å), Fe−OH (1.944 Å), Fe−(OH)−Fe (80.38°), and O−Fe−O (82.84°).

Previous studies[23−25] of $[Fe_2(OH)_3(tmtacn)_2]^{2+}$ have characterized the ion by EXAFS and X-ray diffraction structural techniques and variable-temperature magnetic Mössbauer, EPR, Faraday magnetic-susceptibility, and X-ray L-edge absorption techniques, and have additionally reported the appearance of an intense absorption feature in the near-IR. A combination of EXAFS and X-ray diffraction techniques has determined the cation's structure as an approximately D_{3h} cofacial bioctahedron, having an Fe···Fe separation of ~2.51 Å (Figure 1). Mössbauer spectra in zero magnetic field show a single quadrupole doublet at liquid helium temperatures, indicating the extra electron is delocalized over the two iron sites on the Mössbauer time scale ($\sim 10^{-7}$ s).[23,24] This conclusion is supported by the observation of only one type of Fe in the 10 K L-edge absorption spectrum of this dimer ($\sim 10^{-15}$ s time scale),[25] which indicates that this dimer is firmly in the class III delocalization limit. The magnetic Mössbauer spectra display splittings consistent with an $S = 9/2$ ground state, a result corroborated by the observation of a high-*g* EPR resonance ($g_\perp \approx 10$) and a large high-temperature effective magnetic moment ($\mu_{eff} \approx 10$ B.M.) obtained from magnetic-susceptibility measurements. Analysis of the magnetic Mössbauer spectra yielded spin-Hamiltonian parameters that were interpreted as indicating that the "extra" electron is delocalized along the dimer *z* (Fe···Fe) axis. The room-temperature absorption spectrum of the complex was described as consisting of an intense solvent-independent near-IR feature at ~13 200 cm^{-1}, assigned as the transition between delocalized symmetric and antisymmetric $S = 9/2$ wavefunctions split by $2B(S + 1/2) = 10B$ to give a value of $B = 1320$ cm^{-1}. This, combined with variable-temperature (VT) magnetic Mössbauer, EPR, and magnetic susceptibility experiments allowed an experimental limit of $J > \sim -117.5$ cm^{-1} to be estimated for the Heisenberg ($H = -2JS_1 \cdot S_2$) exchange contribution to the ground-state magnetism.[24]

---

(11) Robin, M. B.; Day, P. *Adv. Inorg. Chem. Radiochem.* **1967**, *10*, 247−403.

(12) Zener, C. *Phys. Rev.* **1951**, *82*, 403−405.

(13) Anderson, P. W.; Hasegawa, H. *Phys. Rev.* **1955**, *100*, 675.

(14) Girerd, J.-J. *J. Chem. Phys.* **1983**, *79*, 1766−1775.

(15) Noodleman, L.; Baerends, E. J. *J. Am. Chem. Soc.* **1984**, *106*, 2316−2327.

(16) Blondin, G.; Girerd, J.-J. *Chem. Rev.* **1990**, *90*, 1359−1376.

(17) Bominaar, E. L.; Hu, Z.; Münck, E.; Girerd, J.-J.; Borshch, S. A. *J. Am. Chem. Soc.* **1995**, *117*, 6976−6989.

(18) Borshch, S. A.; Bominaar, E. L.; Blondin, G.; Girerd, J.-J. *J. Am. Chem. Soc.* **1993**, *115*, 5155−5168.

(19) Noodleman, L.; Case, D. A. *Adv. Inorg. Chem.* **1992**, *38*, 423−470.

(20) Ross, P. K.; Allendorf, M. D.; Solomon, E. I. *J. Am. Chem. Soc.* **1989**, *111*, 4009−4021.

(21) Tuczek, F.; Solomon, E. I. *Inorg. Chem.* **1993**, *32*, 2850−2862.

(22) Brown, C. A.; Remar, G. J.; Musselman, R. L.; Solomon, E. I. *Inorg. Chem.* **1995**, *34*, 688−717.

(23) Drüeke, S.; Chaudhuri, P.; Pohl, K.; Wieghardt, K.; Ding, X.-Q.; Bill, E.; Sawaryn, A.; Trautwein, A. X.; Winkler, H.; Gurman, S. J. *J. Chem. Soc., Chem. Commun.* **1989**, 59−62.

(24) Ding, X.-Q.; Bominaar, E. L.; Bill, E.; Winkler, H.; Trautwein, A. X.; Drüeke, S.; Chaudhuri, P.; Wieghardt, K. *J. Chem. Phys.* **1990**, *92*, 178−186.

(25) Peng, G.; van Elp, J.; Jang, H.; Que, L., Jr.; Armstrong, W. H.; Cramer, S. P. *J. Am. Chem. Soc.* **1995**, *117*, 2515−2519.

In the present study low-temperature (LT) absorption, magnetic circular dichroism (MCD), and resonance Raman (RR) spectroscopies are used to probe the excited-state properties of $[Fe_2(OH)_3(tmtacn)_2]^{2+}$. Spectral assignments allow the development of a detailed molecular-orbital description of bonding in this dimer, in which excited-state splitting patterns are correlated with specific orbital interactions. This bonding description is further supported by spin-unrestricted SCF-Xα-SW calculations. Analysis based on these band assignments provides estimates of superexchange and double-exchange contributions to the ground-state magnetism and defines the specific orbital pathways of each. Analysis of the excited-state splittings provides an estimate of the ground-state J value, and this is compared to a limiting value obtained from VT magnetic-susceptibility experiments. The excited-state spectroscopy of $[Fe_2(OH)_3(tmtacn)_2]^{2+}$ therefore provides a significant experimental test of the double-exchange description of ferromagnetism in mixed-valence dimers. The structural and orbital factors responsible for the ground-state properties of $[Fe_2(OH)_3(tmtacn)_2]^{2+}$ are then discussed in relation to the corresponding properties of half-met Hemerythrin (Hr) and the $[Fe_2S_2]^+$ active sites in "plant-type" ferredoxins and related iron−sulfur clusters.

Experimental Section

X-ray Diffraction. $[C_{18}H_{45}N_6O_3Fe_2][ClO_4]_2 \cdot 2CH_3OH \cdot 2H_2O$, prepared as described in ref 23, crystallizes in the trigonal space group $P3_121$ (no. 152) with cell constants (at −80 °C) $a = b = 14.350$ (3) Å, $c = 18.706$ Å, $V = 3336$ (2) Å^3, $Z = 3$, $F(000) = 1275$, $M = 804.3$, and $\rho_{calcd} = 1.20$ g/cm^3. Cell parameters were obtained from least-squares fits to the settings of 25 reflections in the range $15° \leq \theta \leq 20°$ centered on an Enraf-Nonius CAD4 diffraction by using Mo Kα radiation ($\lambda = 0.710\,73$ Å). Intensities were collected for a crystal with dimensions $0.28 \times 0.16 \times 0.56$ mm^3 at −80 °C for $2\theta \leq 45°$. No significant deviations in intensity were registered for three monitor reflections recorded at regular intervals. A total of 1640 symmetry-independent reflections were collected in the ω mode at scan speeds varying between 1.29 and 6.71 deg/min for scan ranges $0.85 + 0.35 \tan \theta$. On the basis of the rejection criterion, $F_o^2 \leq 3\sigma(F_o^2)$, 1318 reflections were employed for the subsequent refinements. The structure was solved by direct methods and refined by full matrix least squares[26] with anisotropic temperature factors for the non-hydrogen atoms of the anion, cation, and the water oxygen. The asymmetric unit also contains a disordered methanol molecule, the carbon and oxygen atoms of which were assigned a group isotropic temperature factor. Neutral atom scattering factors, corrected for the real and imaginary parts of anomalous dispersion, were taken from ref 27. Corrections for absorption were applied after isotropic least-squares refinement by use of the program DIFABS.[28] The function minimized during the refinement was $\sum w(|F_o| - |F_c|)^2$ with $w = [\sigma^2(F_o) + p^2F_o^2]^{-1}$, $p = 0.014$. Terminal R factors were $R = 0.110$ and $R_w = [\sum w(|F_o| - |F_c|)^2/\sum w|F_o|^2]^{1/2} = 0.108$. Positions for hydrogen atoms were not included in the refinement.

Magnetism. Isofield variable-temperature (0.1 T, 2−300 K) and variable-field high-temperature (0−5 T, 300 K) magnetic-susceptibility measurements were collected on powdered samples of $[Fe_2(OH)_3(tmtacn)_2]^{2+}$ using a Quantum Design MPMS SQUID magnetometer. The magnetometer was calibrated against mercury tetrathiocyanocobaltate(II) and a palladium cylinder. The sample was held firmly in a polycarbonate capsule (Universal Plastics and Engineering Co., Rockville, MD) to prevent crystallite torquing in an applied magnetic field, and the capsule was housed in a clear plastic soda straw fixed to the magnetometer drive rod. Pascal's constants were used to determine the constituent atom diamagnetism.[29−31] The sample holder diamagnetism was measured and subtracted from the raw magnetization data.

Electronic Absorption and Magnetic Circular Dichroism Spectroscopies. Low-temperature absorption data were collected on a Cary-17 spectrophotometer using a Janis Research Super Vari-Temp cryogenic dewar mounted in the optical path. MCD measurements were performed on Jasco J500 (UV/vis/near-IR, S1 and S20 PMT detection) and J200 (near-IR, InSb detection) CD spectropolarimeters with sample compartments modified to accommodate Oxford Instruments SM4-6T and -7T cryogenic superconducting magnetooptical dewars. Samples of $[Fe_2(OH)_3(tmtacn)_2]^{2+}$, dissolved anaerobically in 50:50 propionitrile/butyronitrile solvent mixtures deoxygenated by multiple freeze−pump−thaw cycles, were injected into absorption and MCD sample cells comprised of quartz disks separated by Viton O-ring spacers, and rapidly frozen. Solid samples for absorption and MCD consisted of a suspension of powdered sample in poly(dimethylsiloxane) mulling agent held between quartz disks. MCD samples were checked for depolarization effects prior to each experiment by monitoring the CD signal of a nickel (+)-tartrate solution placed before and after the sample compartment. All samples used for collection of the data presented displayed negligible (<5%) depolarization effects at liquid helium temperatures.

Vibrational and Resonance Raman Spectroscopies. Resonance Raman spectra were obtained using constant wave (CW) excitation from Kr^+ (Coherent I90K) and Ar^+ (Coherent I18UV) ion laser sources. Incident power in the range of 15−75 mW was used in a ∼135° back-scattering arrangement. Scattering was measured using a SPEX Model 1877 CP triple monochromator with 1200, 1800, and 2400 gr/mm holographic gratings equipped with a Princeton Instruments back-illuminated CCD detector. Scattering resolution was ∼1.0 cm^{-1} at all excitation energies. Anaerobic powdered samples diluted with KBr were spun in sealed NMR tubes cooled to ∼120 K using a nitrogen gas flow system. Profile intensities of Raman scattering peaks were determined by integration of background-corrected spectra and quantified relative to the 983.6 cm^{-1} scattering peak of solid K_2SO_4, dispersed isotropically in the NMR tube. Depolarization ratios were measured at room temperature from an anaerobic CH_3CN solution of the sample using the identical optical configuration.

Electronic-Structure Calculations. Electronic-structure calculations were performed using the 1982 QCPE SCF-Xα-SW programs,[32] approximating the tridentate tmtacn ligands by three amine ligands, resulting in the computational model $[Fe_2(OH)_3(NH_3)_6]^{2+}$. Details of the calculation (sphere radii, α values, and atomic positions) are given in the supporting information.

Results

X-ray Diffraction Studies. Figure 1 depicts the results of 198 K X-ray diffraction studies on $[Fe_2(OH)_3(tmtacn)_2](ClO_4)_2$. The cation displays crystallographic C_2 symmetry with an Fe···Fe distance of 2.509(6) Å. The extremely large anisotropic temperature factors of the carbon atoms of the 1,4,7-triazacyclononane ligands indicate the presence of a static disorder in the five-membered chelate rings. Attempts to model this disorder by introducing split positions for the ligand carbon atoms were unsuccessful. As a result of the above disorder, bond lengths and angles from this crystal structure other than the Fe···Fe distance are unreliable. These results are, however, in good agreement with those of previous EXAFS and room-temperature X-ray diffraction studies.[23,24] A description of the crystal structure analysis, including the crystal morphology, is available as supporting information.

Magnetism. The temperature dependence of the effective magnetic moment measured for $[Fe_2(OH)_3(tmtacn)_2]^{2+}$ is shown in Figure 2. The error bars shown on a *ca.* 10-fold-expanded scale in Figure 2 (inset) are estimated from differences between two data sets on different samples and multiple readings at 300

---

[26] Sheldrick, G. M. *SHELX-76*; University of Cambridge: Cambridge, England, 1976.

[27] *International Tables for X-Ray Crystallography*; Kynoch Press: Birmingham, England, 1974; Vol. IV, pp 99−149.

[28] Walker, N.; Stuart, D. *Acta Crystallogr.* **1983**, *A39*, 158−166.

[29] Weller, R. R.; Hatfield, W. E. *J. Chem. Educ.* **1979**, *56*, 652.

[30] *Modern Coordination Chemistry*; Figgis, B. N., Lewis, J., Eds.; Interscience: New York, 1960; p 403.

[31] König, E. *Magnetic Properties of Transition Metal Compounds*; Springer-Verlag: Berlin, 1966.

[32] Cook, M.; Case, D. A. *QCPE Program #465* **1991**, *23*, 21−22.

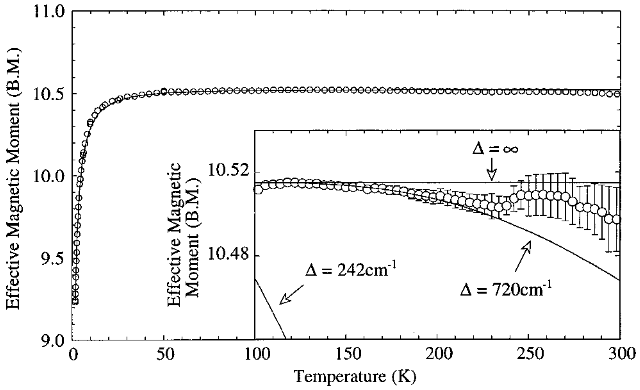

Figure 2. Variable-temperature magnetic-susceptibility data (○) collected at 0.1 T. The solid line is the best fit of the low-temperature data using the model described in the text ($g = 2.115$ and $D = 2.28$ cm^{-1}). Inset: high-temperature magnetic-susceptibility data (○) displayed on an expanded scale. A set of simulated data curves (eq 5) is included showing the calculated temperature dependence as a function of $\Delta_{7/2-9/2}$. A limiting value of $\Delta > \sim 720$ cm^{-1} is concluded (see the text).

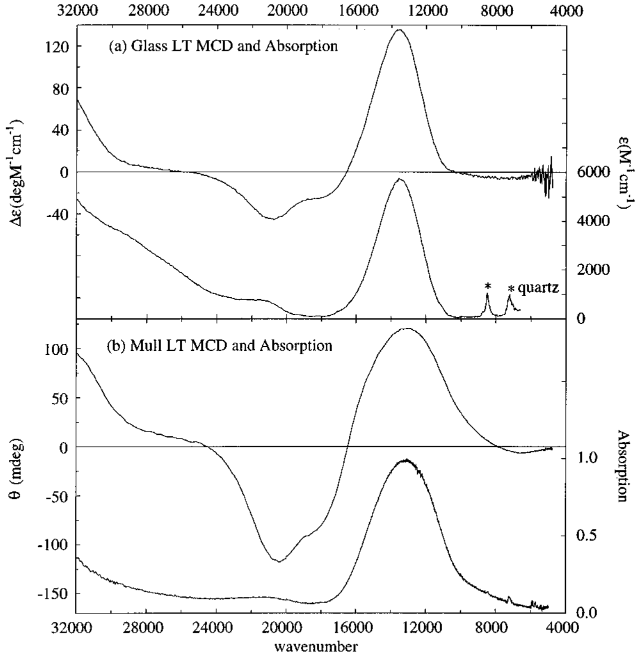

Figure 3. Low-temperature absorption and MCD spectra of $[Fe_2(OH)_3(tmtacn)_2]^{2+}$ in (a) 50:50 propionitrile/butyronitrile glass and (b) solid-state mull.

K. At temperatures above ∼50 K the effective moment is essentially constant at 10.5 B.M. (the spin-only moment for $S = 9/2$ is 9.95 B.M.). At temperatures below ∼50 K the effective moment decreases sharply, indicating the presence of zero-field splitting within the ground-state manifold. High-temperature variable-field (300 K, 0−5 T) magnetic-susceptibility measurements (data not shown) yield a linear magnetization plot.

Electronic Absorption (LT Mull, Glass) and MCD (LT, VTVH). Figure 3 shows the low-temperature absorption and MCD spectra of $[Fe_2(OH)_3(tmtacn)_2]^{2+}$ in both solvated (Figure 3a) and solid mull (Figure 3b) forms. The absorption spectrum of $[Fe_2(OH)_3(tmtacn)_2]^{2+}$ is dominated by an intense ($\epsilon \approx 5700$ M^{-1} cm^{-1}) slightly-asymmetric near-IR feature occurring at $\upsilon_{max} = 13\,500$ cm^{-1} in the glass and $\upsilon_{max} = 13\,130$ cm^{-1} in the solid state. The bandwidth of this absorption feature is observed to diminish significantly upon solvation, decreasing from fwhm ≈ 4450 cm^{-1} in the solid to fwhm ≈ 2880 cm^{-1} in the glass, which is interpreted as reflecting crystallographically-imposed inhomogeneities in the solid state. Also observable in the absorption spectrum is a weaker feature ($\epsilon \approx 750$ M^{-1} cm^{-1}) occurring at 21 350 cm^{-1} in the glass and 21 230 cm^{-1} in the solid state. The MCD spectrum of $[Fe_2(OH)_3(tmtacn)_2]^{2+}$ is depicted in Figure 3, parts a (glass) and b (solid), and shows a large ($\Delta\epsilon \approx 135$ deg M^{-1} cm^{-1}) positive-signed feature occurring at 13 550 cm^{-1} (fwhm ≈ 2960 cm^{-1}) in the glass and 13 110 cm^{-1} (fwhm ≈ 4790 cm^{-1}) in the solid, coinciding with the dominant absorption feature. A negative feature ($\Delta\epsilon \approx -45$ deg M^{-1} cm^{-1}) coinciding with the weaker observed absorption feature is observed at 20 770 cm^{-1} in the glass and 20 410 cm^{-1} in the solid. The MCD spectrum also reveals two additional negative bands that have no corresponding absorption intensity, occurring at 7380 cm^{-1} ($\Delta\epsilon \approx -6$ deg M^{-1} cm^{-1}) and 17 860 cm^{-1} ($\Delta\epsilon \approx -25$ deg M^{-1} cm^{-1}) in the glass and 6 600 and 18 370 cm^{-1} in the solid. Both absorption and MCD spectra show significant intensity occurring at energies greater than 32 000 cm^{-1}.

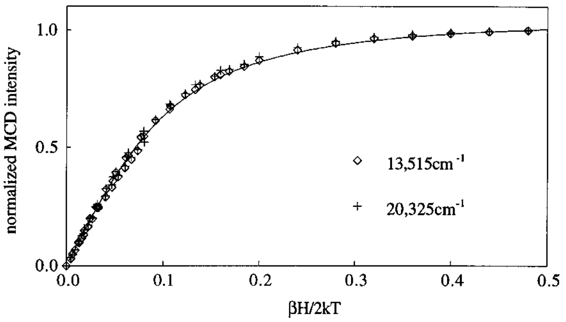

Figure 4. Normalized solid-state variable-temperature variable-field (VTVH) MCD intensity monitored at 13 515 and 20 325 cm^{-1} and at temperatures of 4.2, 10, and 25 K and fields of 0−7 T. The $S = 9/2$ Brillouin function using $g = 2.11$ is superimposed.

All observed MCD intensity displays *C*-term behavior, decreasing in magnitude with increasing temperature: Normalized variable-temperature variable-field (VTVH) MCD intensities of the dominant positive and negative features (monitored at 13 515 and 20 325 cm^{-1} in the mulled sample), plotted in Figure 4 as a function of $\beta H/2kT$, show nearly superimposable isotherms in the temperature range between 4.2 and 25 K. The $S = 9/2$ Brillouin function[33] ($g = 2.11$) superimposed in Figure 4 confirms the $S = 9/2$ saturation behavior of the observed MCD features.

Raman Spectroscopy. In Figure 5, the 120 K solid-state 568 nm preresonance Raman spectra of $[Fe_2(^{16}OH)_3(tmtacn)_2]^{2+}$ and $[Fe_2(^{18}OH)_3(tmtacn)_2]^{2+}$ are compared. Four low-frequency fundamental bands are observed, the two dominant bands at 316.2 and 124.4 cm^{-1} and two smaller bands at 229.1 and 187.5 cm^{-1} (±1.0 cm^{-1}), all of which shift to lower energy upon ^{18}O substitution (308.5, 119.8, 224.1, and 180.8 cm^{-1}). The 120 K solid-state resonance Raman excitation profiles (RREPs) of these bands[34] show dominant enhancement of the 316 and 124 cm^{-1} scattering peaks under the large absorption feature at ∼13 500 cm^{-1} (Figure 3). There is no discernible intensity enhancement under the ∼21 000 cm^{-1} absorption feature, and virtually no observable intensity at 24 585 cm^{-1}, the highest energy Raman data point. Room-temperature CH_3CN solution spectra of $[Fe_2(OH)_3(tmtacn)_2]^{2+}$ (data not shown) give essentially identical vibrational spectra and resonance Raman excitation profiles as in the solid state. Solution depolarization ratios for the 316

---

(33) Kittel, C. *Introduction to Solid State Physics;* 6th ed.; Wiley & Sons: New York, 1986; pp 400−402.

(34) Gamelin, D. R.; Bominaar, E. L.; Mathonière, C.; Kirk, M. L.; Girerd, J.-J.; Wieghardt, K.; Solomon, E. I. *Inorg. Chem.* **1996**, *35*, 4323−4335.

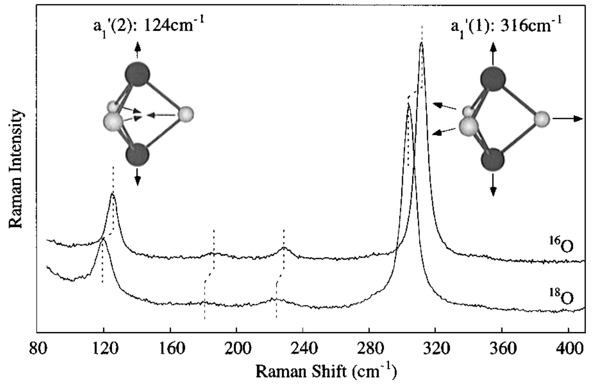

Figure 5. Solid-state Raman scattering of $[Fe_2(^{16}OH)_3(tmtacn)_2]^{2+}$ and $[Fe_2(^{18}OH)_3(tmtacn)_2]^{2+}$ at ~120 K using 568 nm excitation. Included are depictions of the $a_1'(1)$ and $a_1'(2)$ normal mode solutions from a normal coordinate analysis based on the isotopic shifts observed[34] (^{16}O, 316.2, 229.1, 187.5, 124.4 cm^{-1}; ^{18}O, 308.5, 119.8, 224.1, 180.8 cm^{-1} (± 1.0 cm^{-1})).

and 124 cm^{-1} modes are 0.35 ± 0.04 and 0.35 ± 0.05 off resonance (17 606 cm^{-1}) and 0.36 ± 0.04 and 0.38 ± 0.03 on resonance (13 298 cm^{-1}).

Analysis

A. Ground State of $[Fe_2(OH)_3(tmtacn)_2]^{2+}$. Magnetism. Delocalization of the extra electron in this mixed-valence dimer results in a non-Heisenberg spin ladder with energies of symmetric and antisymmetric S_{Tot} levels given by eq 1,[24] where

$$E^{s,a}(S) = -JS(S+1) \pm B(S+1/2) \tag{1}$$

J is the HDVV exchange parameter ($H = -2JS_1 \cdot S_2$) and B is the absolute-value double-exchange parameter. From eq 1, the first thermally-accessible excited spin state ($S = 7/2$) occurs at an energy of $\Delta_{7/2-9/2} = B + 9J$ above the $S = 9/2$ ground state. VT magnetic-susceptibility measurements (Figure 2) on $[Fe_2(OH)_3(tmtacn)_2]^{2+}$ can be used to probe for thermally-accessible excited states with $S < 9/2$, the observation of which would provide an experimental measure of the spin-ladder energies described by eq 1.

The low-temperature region ($T < 150$ K in Figure 2) is analyzed first by assuming population of only the $S = 9/2$ spin state at these temperatures. The Hamiltonian given in eq 2 is

$$H = g_{\|}\beta HS_z + g_{\perp}\beta(H_xS_x + H_yS_y) + D[S_z^{\,2} - (1/3)S(S+1)] \tag{2}$$

used to operate on the ground-state ($|S = 9/2, m_s\rangle$) basis functions. To avoid the concern of overparameterization, the g tensor is treated as isotropic, and this and the axial zero-field splitting (ZFS) parameter, D, are allowed to vary freely. Diagonalization of the resultant matrix yields 10 energy eigenvalues, E_{m_s}, which are substituted into the thermodynamic expression for the magnetic susceptibility:

$$\chi_\theta = \frac{-N}{H}\left[\frac{\displaystyle\sum_{m_s}\frac{\partial E_{m_s}}{\partial H}\exp\left(\frac{-E_{m_s}}{kT}\right)}{\displaystyle\sum_{m_s}\exp\left(\frac{-E_{m_s}}{kT}\right)}\right] \tag{3}$$

In this expression, χ_θ is the molar magnetic susceptibility and θ is the angle between the applied magnetic field and the principle axis of the ZFS tensor. The partial derivatives of the eigenvalues with respect to the applied field, $\partial E_{m_s}/\partial H$, are calculated using the Hellman–Feynman theorem.[35] A numerical-integration method incorporating the Labatto quadrature[36] is used to determine the powder-average molar magnetic susceptibility:[37]

$$\chi_{av} = (1/2)\int_0^{\pi}\chi_\theta \sin\theta \, d\theta \tag{4}$$

The best fit to the $T < 150$ K VT magnetic-susceptibility data (Figure 2) yields the parameters $g_{av} = 2.115$ and $D = 2.28$ cm^{-1}, which are in reasonable agreement with those determined from EPR and magnetic Mössbauer spectroscopies ($g_{\|} = 2.30$, $g_{\perp} = 2.04$, and $D = 1.8$ cm^{-1}).[24]

The dependence of the VT susceptibility behavior on $\Delta_{7/2-9/2}$ can then be calculated using a field-independent Van Vleck model (eq 5) that incorporates the entire spin ladder described by eq 1:

$$\chi_{\text{Van Vleck}} = \frac{\displaystyle N\sum_S\sum_{m_s}\left[\frac{(E^{(1)}_{S,m_s})^2}{kT} - 2E^{(2)}_{S,m_s}\right]\exp\left(\frac{(-E^{(0)}_S)}{kT}\right)}{\displaystyle\sum_S(2S+1)\exp\left(\frac{(-E^{(0)}_S)}{kT}\right)} \tag{5}$$

where $E^{(0)}_S$ is the energy of an excited spin state, S, in zero applied field relative to the $S_T = 9/2$ (symmetric) ground state, obtained from eq 1 (*i.e.*, $\Delta_{S-9/2}$), $E^{(1)}_{S,m_s} = [g^2\beta^2[S(S+1)(2S+1)]/3]^{1/2}$ is the first-order Zeeman coefficient, $E^{(2)}_{S,m_s}$ is the second-order Zeeman coefficient (taken as zero due to the small off-diagonal Zeeman matrix elements in the low $H_{applied}$ limit), and β is the Bohr magneton. Using the experimental values of $B = 1350$ cm^{-1} obtained from the low-temperature absorption spectrum (*vide infra*) and g = 2.115 from the low-temperature susceptibility fit of the same data set, simulations of the high-temperature data (shown in Figure 2 (inset) on an expanded scale with error bars) provide a lower limit of $\Delta_{7/2-9/2} > \sim 720$ cm^{-1}, which corresponds to a limiting value of $J > \sim -70$ cm^{-1}. This limit corresponds to <2% $S = 7/2$ population at 300 K. For comparison, Figure 2 (inset) also shows the temperature dependence calculated for $\Delta_{7/2-9/2}$ values of infinity (zero population of the $S = 7/2$ state) and 242 cm^{-1} (the lower limit for $\Delta_{7/2-9/2}$ obtained from VT EPR and magnetic Mössbauer experiments[24]). From this analysis it is apparent that for $\Delta_{7/2-9/2} > \sim 720$ cm^{-1} (J less antiferromagnetic) the VT-susceptibility curves become increasingly indistinguishable, while for $\Delta_{7/2-9/2} < \sim 720$ cm^{-1} (J more antiferromagnetic) a greater deviation from linearity with increasing temperature would occur than is experimentally observed. High-temperature magnetization experiments (data not shown) are consistent with this conclusion: The linear 0–5 T magnetization curve obtained at 300 K yields a value of $g_{av} = 2.0 \pm 0.2$ when analyzed assuming only $S = 9/2$ population and does not require population of a thermally-excited $S = 7/2$ state to obtain a g-value within experimental error of that determined from the low-temperature susceptibility data ($g_{av} = 2.115$, Figure 2). In summary, analysis of the VT magnetic-susceptibility data allows the conclusion that any antiferromagnetic Heisenberg contribution to the ground-state magnetism of $[Fe_2(OH)_3(tmtacn)_2]^{2+}$ must be smaller in magnitude than $|J| \approx 70$ cm^{-1}.

---

[35] Vermaas, A.; Groeneveld, W. L. *Chem. Phys. Lett.* **1974**, *27*, 583–585.

[36] Scarborough, J. P. *Numerical Mathematical Analysis*; Oxford University Press: New York, 1971; p 159.

[37] Marathe, V. R.; Mitra, S. *Chem. Phys. Lett.* **1974**, *27*, 103–106.

Table 1. Ground-State Geometric Parameters, a_1' Core Vibrational Normal Coordinates, and σ–σ^* Excited-State Geometric Distortion of $[Fe_2(OH)_3(tmtacn)_2]^{2+}$ [34]

		ground-state vibrational normal coordinates (Q_n)		
int coord	ground-state geometry	$+a_1'(1)$: 316 cm^{-1}	$+a_1'(2)$: 124 cm^{-1}	excited-state distortion[a] (++)
Fe···Fe	2.509 Å	0.1424	0.1246	+0.38Å
Fe–OH	1.944 Å	0.1164	−0.0403	+0.10Å
Fe–O–Fe	80.38°	−0.0052	0.1189	+0.169 (+9.4°)
O–Fe–O	82.84°	0.0039	−0.0886	−0.126 (−7.1°)
Displacement from Origin with Excitation (Å)				
Fe			+0.19 Å	
O			−0.04 Å	
(ratio Fe:O)			(+4.9:−1.0)	

[a] Based on distortion parameters obtained from simulation of the variable-temperature absorption and resonance Raman excitation profile data, and Xα-SW calculations.[34]

Molecular Vibrations. The resonance-enhanced vibrations observed in $[Fe_2(OH)_3(tmtacn)_2]^{2+}$ (Figure 5) have been assigned on the basis of their frequencies and isotopic sensitivity.[34] The two dominantly enhanced vibrations are assigned as the totally-symmetric in-phase "breathing" (316 cm^{-1}) and out-of-phase "accordion" (124 cm^{-1}) modes, and descriptions of these two modes calculated from a normal coordinate analysis[34] are given in Table 1 and depicted above the Raman scattering peaks in Figure 5. Note that $a_1'(1)$ and $a_1'(2)$ are the only normal modes of the $Fe(O')_3Fe$ core that involve the Fe···Fe nuclear coordinate.

B. Excited States of $[Fe_2(OH)_3(tmtacn)_2]^{2+}$. D_{3h} Molecular-Orbital Diagram. The electronic structures of D_{3h} M_2L_9 cofacial-bioctahedral complexes have been studied using a variety of calculational[38–42] and spectroscopic[43–45] approaches. On the basis of these studies, a qualitative dimer molecular-orbital energy diagram can be composed for $[Fe_2(OH)_3(tmtacn)_2]^{2+}$ that delineates the effects of both metal–ligand and metal–metal interactions in a cofacial-bioctahedral geometry. For use in this analysis the trigonally-quantized single-site d orbitals are expressed as linear combinations of the octahedral d-orbital basis set:[46,47]

$$t_{2g}:\quad |z^2\rangle,\quad \frac{1}{\sqrt{3}}(\sqrt{2}|x^2-y^2\rangle - |xz\rangle),\quad \frac{1}{\sqrt{3}}(\sqrt{2}|xy\rangle + |yz\rangle) \tag{6}$$

$$e_g:\quad \frac{1}{\sqrt{3}}(|x^2-y^2\rangle + \sqrt{2}|xz\rangle),\quad \frac{1}{\sqrt{3}}(|xy\rangle - \sqrt{2}|yz\rangle)$$

where the iron atomic z axes are oriented along the Fe···Fe axis. The resulting diagram is presented in Figure 6a. The left side of the molecular-orbital diagram represents the monomeric octahedral ligand-field splitting (10 Dq) of the two trigonally-quantized halves of the dimer. Upon dimerization the t_{2g} and e_g degeneracies are broken by perturbations in metal–bridge bonding interactions as a result of the reduction from O_h mononuclear to D_{3h} dimer symmetry (Figure 6a, left center, *vide infra*). These dimer orbitals are further perturbed by σ, π, and δ bonding interactions with the d orbitals of the second iron (Figure 6a, center, *vide infra*). Representative bonding interactions are depicted schematically in Figure 6b for the symmetric and antisymmetric combinations of d_{z^2} orbitals. $[Fe_2(OH)_3(tmtacn)_2]^{2+}$ has 11 valence electrons that are distributed in the lowest-energy high-spin configuration as shown in Figure 6a (center), giving a $s = 9/2$ ground state, consistent with the results from the ground-state magnetic studies. From this ground state, only a_1' to a_2'' and e' one-electron promotions are electric-dipole-allowed, and thus only these are expected to show any significant absorption intensity. The predicted electric-dipole-allowed electronic excitations and their polarizations are indicated in Figure 6a (right). From this diagram, one z-polarized ($a_1'(t_{2g}) \rightarrow a_2''(t_{2g})$) and two x,y-polarized ($a_1'(t_{2g}) \rightarrow e'(t_{2g})$, $e'(e_g)$) transitions are anticipated in the electronic absorption spectrum.

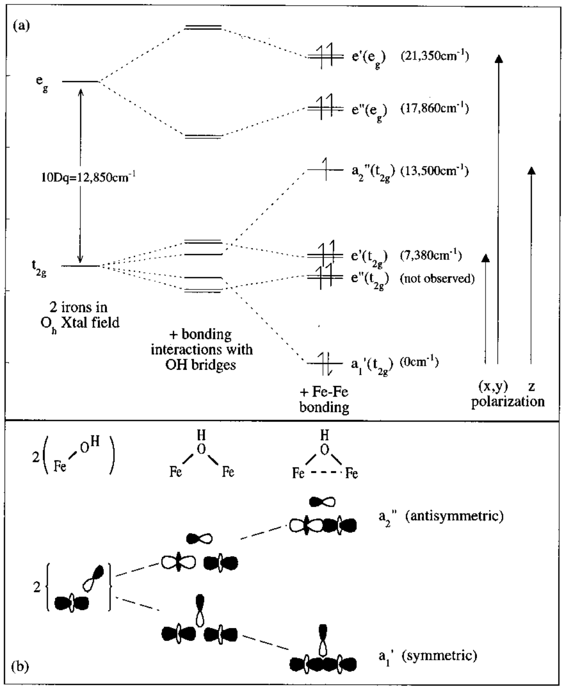

Figure 6. (a) Molecular-orbital splitting diagram for $[Fe_2(OH)_3(tmtacn)_2]^{2+}$ based on the observed electronic spectra and eq 7a–f. The center panel is scaled to match experimental numbers (in parentheses), and an intermediate solution ($e_\sigma^M/e_\pi^M = 5$, $x_H = 1$) of eq 7 has been used to generate the splitting patterns. Also depicted are the allowed electric-dipole transitions based on D_{3h} selection rules (right). (b) Schematic depiction of the orbital interactions responsible for splitting the $a_1'(t_{2g})$ and $a_2''(t_{2g})$ molecular orbitals in (a).

Band Assignments. Two absorption features are observed in the energy region between 5000 and 25 000 cm^{-1}, occurring at 13 500 and 21 300 cm^{-1} (Figure 3). As described in the Results, large Raman intensity enhancement is observed for the ^{18}O-sensitive $a_1'(1)$ and $a_1'(2)$ $[Fe_2(OH)_3]^{2+}$ modes as the excitation energy is tuned through the absorption feature at 13 500 cm^{-1}. The solution depolarization ratios for the $a_1'(1)$ and $a_1'(2)$ vibrational scattering peaks at the enhancement maximum are approximately one-third, indicating the enhancement derives from a singly-degenerate excited state,[48] of which there is only one (Figure 6a, center). The dominant absorption

---

(38) Medley, G. A.; Stranger, R. *Inorg. Chem.* **1994**, *33*, 3976–3985.
(39) Natkaniec, L. *Bul. Acad. Pol. Sc.* **1978**, *26*, 633–640.
(40) Summerville, R. H.; Hoffmann, R. *J. Am. Chem. Soc.* **1979**, *101*, 3821–3831.
(41) Leuenberger, B.; Güdel, H. U. *Inorg. Chem.* **1986**, *25*, 181–184.
(42) Natkaniec, L. *Bull. Acad. Pol. Sci.* **1978**, *26*, 625–631.
(43) Hush, N. S.; Beattie, J. K.; Ellis, V. M. *Inorg. Chem.* **1984**, *23*, 3339–3342.
(44) Riesen, H.; Reber, C.; Güdel, H. U.; Wieghardt, K. *Inorg. Chem.* **1987**, *26*, 2747–2750.
(45) Stranger, R.; Moran, G.; Krausz, E.; Medley, G. *Inorg. Chem.* **1993**, *32*, 4555–4560.
(46) Ballhausen, C. J. *Introduction to Ligand Field Theory*; McGraw-Hill: New York, 1962.
(47) Trogler, W. C. *Inorg. Chem.* **1980**, *19*, 697–700.
(48) Mortensen, O. S.; Hassing, S. In *Advances in Infrared and Raman Spectroscopy*; Clark, R. J., Hester, R. E., Eds.; Heyden: London, 1979; Vol. 6, pp 1–60.

feature at 13 500 cm^{-1} is therefore assigned as the *z*-polarized $a_1'(t_{2g}) \rightarrow a_2''(t_{2g})$ transition, which involves a one-electron promotion between related symmetric and antisymmetric molecular orbitals having octahedral t_{2g} d orbital parentage. From this splitting and eq 1, $\Delta E^{s,a}(9/2) = 10B = 13\,500$ cm^{-1}, and the magnitude of the double-exchange parameter, *B*, is thus determined to be 1350 cm^{-1}. The higher energy absorption feature ($\upsilon_{max} \approx 21\,300$ cm^{-1}) is then assigned as the electric-dipole-allowed *x,y*-polarized $a_1'(t_{2g}) \rightarrow e'(e_g)$ transition. This transition involves electron promotion to a molecular orbital originating from the e_g set of d orbitals, which is split in the dimer by metal−bridge and/or metal−metal interactions. The relative absorption intensities of these two dipole-allowed transitions are consistent with their assignments and result from the large difference in Fe−Fe overlap between the dimer orbitals involved in each transition ($d_{z^2} + d_{z^2}$ to $d_{z^2} - d_{z^2}$ versus $d_{z^2} + d_{z^2}$ to $d_{\pi,\delta} + d_{\pi,\delta}$). The MCD spectrum of $[Fe_2(OH)_3(tmtacn)_2]^{2+}$ (Figure 3) shows two additional bands not observed in the absorption spectrum that can be assigned on the basis of the molecular-orbital scheme in Figure 6a. The higher of these occurs as a negative shoulder at ∼18 000 cm^{-1} and is assigned as the transition to the second molecular orbital having e_g parentage, namely, the formally electric-dipole-forbidden $a_1'(t_{2g}) \rightarrow e''(e_g)$ one-electron promotion, on the basis of its energy and lack of absorption intensity. The very weak low-energy negative MCD feature observed at ∼7000 cm^{-1} is then one of the $a_1'(t_{2g}) \rightarrow e'(t_{2g})$ or $e''(t_{2g})$ transitions and is assigned as the $a_1'(t_{2g}) \rightarrow e'(t_{2g})$ promotion on the basis of angular overlap and Xα-SW calculations (*vide infra*). The band assignments are summarized in Figure 6a (center).

The MCD intensity of this dimer shows *C*-term temperature-dependent behavior (Figure 4). Expansion of the *C*-term MCD intensity expression[49] yields a sum of three contributions, each of which is a product of a Zeeman operator and electric-dipole matrix elements in two directions orthogonal to the Zeeman direction (*i.e.*, $\Delta\epsilon \; \alpha \; g_zM_xM_y + g_xM_yM_z + g_yM_xM_z$). From the transition-dipole polarizations given in Figure 6a (right), only the $a_1' \rightarrow e'$ transitions are dipole allowed in two perpendicular directions (*x* and *y*), and thus only these should show *C*-term MCD intensity in the limit of pure polarized transitions. Formally-degenerate excited states such as in the $a_1' \rightarrow e'$ transitions generally obtain MCD *C*-term intensity from excited-state in-state spin−orbit coupling, which splits coupled spinor components of the excited state and leads to characteristic derivative-shaped pseudo-*A*-term MCD features.[49] The observation of only negative MCD intensity associated with the $a_1'(t_{2g}) \rightarrow e'(e_g)$ transition (Figure 3), and comparable positive MCD intensity attributable to the formally *z*-polarized $a_1'(t_{2g}) \rightarrow a_2''(t_{2g})$ transition, is therefore indicative of out-of-state spin−orbit coupling involving these energetically-similar excited states.[50,51] MCD intensities derived from out-of-state spin−orbit coupling between excited states follow the "sum rule", such that the integrated positive and negative intensities sum to zero if transitions to all of the participating excited states are in the measured spectral region.[50,51] The ratios of integrated positive to negative intensity in the energy region below ∼25 000 cm^{-1} of Figure 3 are approximately 1.8:−1.0 in frozen solution and 1.0:−1.0 in the solid state, with all of the positive intensity attributable to the *z*-polarized $a_1'(t_{2g}) \rightarrow a_2''(t_{2g})$ transition and the majority of the negative intensity in the *x,y*-polarized $a_1'(t_{2g}) \rightarrow e'(e_g)$ transition. These relative intensities thus indicate that out-of-state spin−orbit coupling between the $a_1'(t_{2g}) \rightarrow a_2''(t_{2g})$ and $a_1'(t_{2g}) \rightarrow e'(e_g)$ excited states is the dominant source of MCD intensity for the formally *z*-polarized $a_1'(t_{2g}) \rightarrow a_2''(t_{2g})$ transition.

Experimental Estimates of Fe−Fe and Fe−OH Bonding Interactions. The band assignments summarized in Figure 6a may now be used to obtain experimental estimates of the dominant bonding interactions in $[Fe_2(OH)_3(tmtacn)_2]^{2+}$ using an angular overlap model (AOM). The ligand-field splitting, $\Delta = 10$ Dq (Figure 6a, left), for the mixed-valence iron sites can be estimated from the difference between the average energy of the e_g orbitals, experimentally determined to be ∼19 600 cm^{-1}, and the average energy of the t_{2g} orbitals, experimentally determined from the $a_1'(t_{2g})-a_2''(t_{2g})$ splitting to be ∼6750 cm^{-1}, yielding a value of 10 Dq ≈ 12 850 cm^{-1}. The similarity of this value to those of $Fe(H_2O)_6^{2+}$ (10 Dq ≈ 10 400 cm^{-1}) and $Fe(H_2O)_6^{3+}$ (10 Dq ≈ 13 700 cm^{-1})[52] lends support to the approximate molecular-orbital diagram of Figure 6a. The molecular-orbital splittings can be further evaluated using specific AOM parameters describing Fe−OH and Fe−Fe σ-, π-, and δ-bonding.[42] The AOM energies, E_i, of the cofacial bioctahedron's one-electron molecular-orbitals $i = a_1'(t_{2g})$, $a_2''(t_{2g})$, $e'(t_{2g})$, $e''(t_{2g})$, $e'(e_g)$, and $e''(e_g)$ are described as combinations of metal−ligand and metal−metal orbital-interaction energies, *e*, derived from diagonalization of secular equations based on the trigonally-quantized metal (eq 6) and bridging-ligand orbital basis sets:

$$t_{2g} \text{ parentage:} \quad E_{a_1'(t_{2g})} = -\frac{2}{5}\Delta - \frac{2x_H}{3}e^b_{\pi p} - e^M_\sigma \tag{7a}$$

$$E_{a_2''(t_{2g})} = -\frac{2}{5}\Delta + \frac{2}{3}e^b_{\pi p} + e^M_\sigma \tag{7b}$$

$$E_{e'(t_{2g})} = -\frac{2}{5}\Delta + \frac{4}{3}e^b_{\pi p} - \frac{1}{3}e^M_\pi - \frac{2}{3}e^M_\delta \tag{7c}$$

$$E_{e''(t_{2g})} = -\frac{2}{5}\Delta - \frac{4}{3}e^b_{\pi p} + \frac{1}{3}e^M_\pi + \frac{2}{3}e^M_\delta \tag{7d}$$

$$e_g \text{ parentage:} \quad E_{e'(e_g)} = \frac{3}{5}\Delta + \frac{3}{2}e^b_{\sigma s} + \frac{x_H}{2}e^b_{\sigma p} - \frac{2}{3}e^M_\pi - \frac{1}{3}e^M_\delta \tag{7e}$$

$$E_{e''(e_g)} = \frac{3}{5}\Delta - \frac{3}{2}e^b_{\sigma s} - \frac{1}{2}e^b_{\sigma p} + \frac{2}{3}e^M_\pi + \frac{1}{3}e^M_\delta \tag{7f}$$

where $e^b_{\sigma s}$ and $e^b_{\sigma p}$ refer to the energies of σ*-interactions between Fe d orbitals and the s and p orbitals of the bridging OH ligands, respectively, and $e^b_{\pi p}$ refers to the energy of a π*-type interaction between an Fe d orbital and the p orbitals of the bridging OH ligands. The *e* parameters in eqs 7a−f are thus defined as energies of antibonding interactions and as such are always positive. The variable x_H in eqs 7a and 7e is included to modify the contribution to Fe−O interactions of the oxygen p orbital involved in σ-bonding with the hydroxide proton and has a value between zero and one, where zero corresponds to the strong O−H bonding limit. By group theory, the symmetry-adapted linear-combination orbitals of this oxygen p orbital are of $a_1'(\pi)$ and $e'(\sigma)$ symmetry, and thus only the $a_1'(t_{2g})$ and $e'(e_g)$ molecular orbitals contain hydroxide proton contributions. The energy differences between related pairs of molecular orbitals follow from eqs 7a−f:

---

[49] Piepho, S. B.; Schatz, P. N. *Group Theory in Spectroscopy*; Wiley-Interscience: New York, 1983.

[50] Dubicki, L.; Ferguson, J. *Chem. Phys. Lett.* **1984**, *109*, 128−131.

[51] Gerstman, B. S.; Brill, A. S. *J. Chem. Phys.* **1985**, *82*, 1212−1230.

[52] Schläfer, H. L.; Glieman, G. *Basic Principles of Ligand Field Theory*; Wiley-Interscience: London, 1969; p 78.

$$\Delta E_{a_2''(t_{2g})-a_1'(t_{2g})} = \frac{2(x_H + 1)}{3} e^b_{\pi p} + 2e^M_\sigma \qquad (8a)$$

$$\Delta E_{e'(t_{2g})-e''(t_{2g})} = \left(\frac{8}{3} e^b_{\pi p}\right) - \left(\frac{2}{3} e^M_\pi + \frac{4}{3} e^M_\delta\right) \qquad (8b)$$

$$\Delta E_{e'(e_g)-e''(e_g)} = \left(3e^b_{\sigma s} + \frac{1}{2}(x_H + 1)e^b_{\sigma p}\right) - \left(\frac{4}{3} e^M_\pi + \frac{2}{3} e^M_\delta\right) \qquad (8c)$$

The metal−metal AOM parameters are directly related to the parent basis functions as

$$e^M_\alpha = \frac{1}{2}|E(\phi_A + \phi_B) - E(\phi_A - \phi_B)| \qquad (9)$$

$$\phi = |z^2\rangle \text{ for } \alpha = \sigma$$

$$\phi = |xz\rangle \text{ or } |yz\rangle \text{ for } \alpha = \pi$$

$$\phi = |x^2 - y^2\rangle \text{ or } |xy\rangle \text{ for } \alpha = \delta$$

where A and B refer to the two iron centers.

Using these relationships, the energetic splittings of Figure 6a may be quantitated within the AOM formalism. The experimental observables do not allow for unique solution of all parameters and require estimation of the relative magnitudes of the direct metal−metal orbital interaction energies. On the basis of orbital overlap considerations the metal−metal interaction energies follow the relative ordering: $e^M_\sigma > e^M_\pi >> e^M_\delta$. At the 2.51 Å Fe···Fe separation in $[Fe_2(OH)_3(tmtacn)_2]^{2+}$ metal−metal δ-interactions can be neglected and the solution space defined by estimating the σ:π ratio to be in the range of $10 > e^M_\sigma/e^M_\pi > 1$. The AOM parameters derived from the experimentally observed splitting energies of Figure 6a using this range and varying x_H from 0 to 1 are e^M_σ = 5516−6538 cm^{-1}, e^M_π = 633−6085 cm^{-1}, $(3/2)e^b_{\sigma s} + [(x_H + 1)/4]e^b_{\sigma p}$ = 2167−5802 cm^{-1}, and $e^b_{\pi p}$ = 636−1994 cm^{-1}. From these values it is possible to describe each of the pairwise energy splittings shown in Figure 6a in terms of their relative metal−metal and metal−ligand contributions, providing insight into the orbital origins of the observed spectral features. Using this range of solutions, the 13 500 cm^{-1} $a_1'(t_{2g})$−$a_2''(t_{2g})$ orbital splitting (eq 8a) is found to be ∼82−97% attributable to a direct Fe−Fe σ−σ* interaction, while Fe−OH π-interactions contribute only ∼3−18% of this splitting. The low energy of the a_1' orbital relative to the other t_{2g} d orbitals (Figure 6) is therefore not due to the local ligand-field environment of the monomeric Fe sites but rather to a resonance interaction between the two metals in the dimer. Alternatively, the splittings of the e′ and e″ pairs of e_g and t_{2g} parentage are both found to be dominated by Fe−OH interactions. In the e_g set, the $e'(e_g) > e''(e_g)$ order observed experimentally (Figure 6a) is the opposite of that obtained from dominant metal−metal π-interactions (eq 8c). This 3490 cm^{-1} splitting is largely due to Fe−OH σ-bonding interactions (4330−11600 cm^{-1}), with a smaller opposing Fe−Fe π-bonding contribution (−840 to −8110 cm^{-1}). The magnitude of the dominant Fe−OH σ-bonding contribution is thus estimated to be ∼1.4−5.1 times greater than that of Fe−Fe π-bonding. From the parameters in eqs 7c−f, the experimentally determined order of the $e'(e_g)$ and $e''(e_g)$ energies requires the same orbital ordering within the t_{2g} set, thus allowing the observed feature at 7380 cm^{-1} to be associated specifically with the $e'(t_{2g})$ orbital. The t_{2g} e′−e″ molecular-orbital splitting (eq 8b) is due largely to Fe−OH π-interactions (1700−5320 cm^{-1}) with opposing Fe−Fe π-interactions (−420 to −4060) that reduce the splitting. The Fe−OH π contribution to the $e'(t_{2g})$−$e''(t_{2g})$ splitting energy is therefore ∼1.3−4.0 times greater than that of direct Fe−Fe π-interaction. In summary, the approximate AOM treatment of the observed spectral features indicates that greater than ∼80% of the $a_1'(t_{2g})$−$a_2''(t_{2g})$ splitting energy is due to a direct Fe−Fe σ-interaction involving the d_{z^2} orbitals of the two iron atoms, while the e′−e″ splittings within the t_{2g} and e_g d orbital sets are dominated by Fe−OH π- and σ-interactions.

Xα-SW Calculated Wavefunctions and Transition Energies. The results of the electronic-structure analysis of $[Fe_2(OH)_3(tmtacn)_2]^{2+}$ presented above are complemented by SCF-Xα-SW calculations, which further describe the bonding features of this molecule. The calculated d-based molecular wave function distributions and transition-state energies are presented in Table 2, and the associated contours are shown in Figure 7. Also included in Table 2 are the single-site d orbital contributions to each molecular orbital estimated from the Fe inner-sphere descriptions and expressed as linear combinations of the octahedral d orbitals. The total d orbital contribution to each molecular orbital is then described by the symmetric (′) or antisymmetric (″) combination of two mononuclear subunits with the same single-site contributions. The Xα-SW-predicted d−d transition energies (Table 2) are in general agreement with the experimental values and band assignments presented in Figure 6a (center), and predict splitting of the t_{2g} orbitals into a_1'−a_2'' and e′−e″ pairs. In particular, the energy of the $a_1'(t_{2g}) \rightarrow a_2''(t_{2g})$ excitation is calculated to be 13 300 cm^{-1}. This is very similar to the experimental value of 13 500 cm^{-1} and suggests that the calculation models the bonding changes accompanying this electron promotion well. The Xα-SW calculation describes the $a_1'(t_{2g})$ molecular orbital, which contains the extra electron in the ground-state configuration, as a symmetric combination of Fe d_{z^2} orbitals with little bridging-ligand ($O(p_{x,y})$ + H) contribution (∼6% total O + H, Table 2), and calculates a significant σ-bonding overlap between the two d_{z^2} orbitals (Figure 7d). The $a_2''(t_{2g})$ molecular orbital (Figure 7a) consists of the corresponding antisymmetric σ*-antibonding combination of d_{z^2} orbitals with minor bridging-ligand ($O(p_z)$) contributions (∼7%, Table 2). The calculation overestimates the magnitude of metal−metal π-interactions and predicts the $e'(e_g)$ orbital higher in energy than the $e''(e_g)$ orbital, in contrast with the experimental result.[53] In summary, the SCF-Xα-SW calculations, when calibrated to experiment (Figure 6a (center)), provide useful descriptions (Figure 7) of the $[Fe_2(OH)_3(tmtacn)_2]^{2+}$ molecular orbitals not available from the angular overlap analysis, and in particular clearly emphasize the Fe−Fe $\sigma \rightarrow \sigma$* nature of the $a_1'(t_{2g}) \rightarrow a_2''(t_{2g})$ one-electron excitation (Figure 7a,d).

Excited-State Splittings and Ground-State Heisenberg Exchange. The excited-state spectroscopies (Figure 3) allow evaluation of the antiferromagnetic superexchange pathways contributing to J in the $[Fe_2(OH)_3(tmtacn)_2]^{2+}$ ground state. The specific orbitals responsible for exchange coupling of the unpaired spins on each side of this dimer are the $e''(t_{2g})$, $e'(t_{2g})$, and $e''(e_g)$, $e'(e_g)$ molecular-orbital pairs shown in Figure 7, parts b, e and c, f, respectively. As shown in Figure 6, the splittings of e′ and e″ orbitals in this dimer are dominated by metal−ligand antibonding interactions rather than direct metal−metal interactions, and these splittings reflect superexchange antiferromagnetic contributions to the ground-state magnetism. The magnitudes of these contributions may be estimated from the experimental excited-state splittings based on Anderson's

---

[53] This overestimation is reflected in the hybridization of the two e′ dimer orbitals (Table 2), which deviate from the trigonal limit of eq 6 and approach the axial limit in which metal−metal π-bonding is optimized.

Table 2. Xα-SW-Calculated Transition-State Energies and Wavefunction Descriptions of Each d-Based Molecular Orbital in $[Fe_2(OH)_3(NH_3)_6]^{2+}$

molecular orbital	transition-state energy (cm^{-1})	molecular orbital distribution				Fe d orbital contributions[a]
		% Fe[b]	% O	% H	%NH_3	
$e''(e_g)$	25 011	72	13	0	14	67% xz, 33% x^2-y^2
$e'(e_g)$	23 204	76	6	3	15	79% xz, 21% x^2-y^2
$a_2''(t_{2g})$	13 300	91	7	0	2	100% z^2
$e'(t_{2g})$	10 719	80	19	0	2	18% xz, 82% x^2-y^2
$e''(t_{2g})$	6 380	97	1	0	2	35% xz, 65% x^2-y^2
$a_1'(t_{2g})$		93	3	3	2	100% z^2

[a] Only one component of each doubly-degenerate pair is given. [b] All Fe contributions are greater than ~97% d orbital.

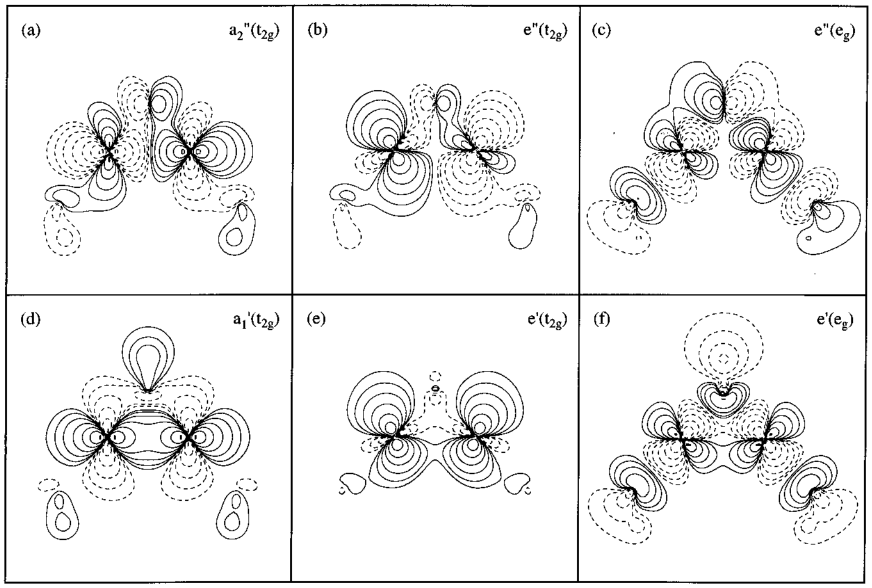

Figure 7. SCF-Xα-SW wave function-amplitude contour plots of the six d-based molecular orbitals of $[Fe_2(OH)_3(NH_3)_6]^{2+}$ (Table 2). All plots are of an Fe−(OH)−Fe plane with contour values of ±0.64, ±0.32, ±0.16, ±0.08, ±0.04, ±0.02, and ±0.01 $(e/bohr^3)^{1/2}$. Note that the oxygen p(π) contribution to the $e'(t_{2g})$ molecular orbital (panel e) is oriented perpendicular to the Fe−(OH)−Fe plane.

exchange theory.[54] This approach has been applied in the study of several multiply-bridged transition metal dimers,[41,55] yielding reasonable values both in absolute magnitudes and in trends across related dimers. Using the treatment of Hay, Thibeault, and Hoffmann,[55] the Heisenberg exchange coupling constant, J, is described as a sum of antiferromagnetic and ferromagnetic contributions:

$$J = J_{AF} + J_F \tag{10}$$

$$J_{AF} = -\frac{1}{m^2}\sum_{i=1}^{m}\frac{(\Delta E_i^{sa})^2}{2(J_{ai,ai} - J_{ai,bi})}$$

$$J_F = \frac{1}{m^2}\sum_a\sum_b K_{ab} = K_{ab}^{av}$$

where m is the number of unpaired electrons on each metal, ΔE^{sa} is the pairwise energy splitting between related symmetric and antisymmetric combination molecular orbitals, and the sum is over all such pairs of orbitals. J_{aa} and J_{ab} are one- and two-site Coulombic repulsion integrals, respectively, and their difference is estimated conservatively to be in the range of 5−15 eV for d electrons in transition-metal coordination complexes.[41,55] In $[Fe_2(OH)_3(tmtacn)_2]^{2+}$ all symmetric and antisymmetric d orbital pairs contribute to Heisenberg exchange coupling except those involving the d_{z^2} orbitals (*i.e.*, $m = 4$). Using eq 10, the experimental energy splittings of $\Delta E^{sa}_{e(e_g)} = 3490\ cm^{-1}$ and $\Delta E^{sa}_{e(t_{2g})} = 1680\ cm^{-1}$ yield an antiferromagnetic superexchange contribution in the range $J_{AF} = -23$ to $-8\ cm^{-1}$. The ferromagnetic contribution, J_F, is expected to be small[41,55] (estimated here as $K_{ab}^{av} \approx 1-10\ cm^{-1}$). Thus, the splittings observed in the excited-state spectroscopy allow a value of $-23\ cm^{-1} \leq J \leq +2\ cm^{-1}$ to be estimated for the combined contributions of all Heisenberg exchange interactions in $[Fe_2(OH)_3(tmtacn)_2]^{2+}$.[56] Using this range and $B = 1350\ cm^{-1}$, the $S = 9/2$ to $S = 7/2$ spin-state energy separation in $[Fe_2(OH)_3(tmtacn)_2]^{2+}$ is calculated to be $1150\ cm^{-1} \leq \Delta_{7/2-9/2} \leq 1400\ cm^{-1}$, which is within the limit of $\Delta > 720\ cm^{-1}$ determined by VT magnetic susceptibility measurements (Figure 2, inset). The excited-state splittings thus support the conclusion from the magnetic susceptibility analysis in indicating a small Heisenberg superexchange contribution to the ground-state magnetism of $[Fe_2(OH)_3(tmtacn)_2]^{2+}$.

***σ*−*σ**Excited-State Distortion.** A detailed understanding of the bonding interactions responsible for splitting the $a_1'(t_{2g})$ and $a_2''(t_{2g})$ molecular orbitals (Figure 6) will provide valuable insight into the origins of this dimer's ground-state properties, including the strong ferromagnetism and valence delocalization, since this splitting determines the dimer's ground-state electronic configuration (Figure 6) and the magnitude of the double-exchange parameter, B (from $\Delta E_{a_2''(t_{2g})-a_1'(t_{2g})} = 10B$, eq 1).

---

(54) Anderson, P. W. *Solid State Phys.* **1963**, *14*, 99−214.

(55) Hay, P. J.; Thibeault, J. C.; Hoffmann, R. *J. Am. Chem. Soc.* **1975**, *97*, 4884−4899.

(56) This analysis is based on the approximation that Fe···Fe d orbital interactions occur only between related orbitals on the two metals. If cross interactions occur, the pair splittings are perturbed and no longer relate directly to the Heisenberg exchange coupling constant, J, as described by eq 10. These perturbations are expected to be small in $[Fe_2(OH)_3(tmtacn)_2]^{2+}$ on the basis of orbital-overlap considerations.

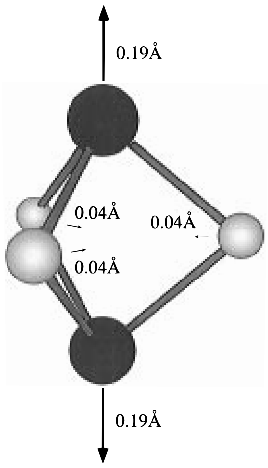

Figure 8. Depiction of the excited-state distortion involved in the $a_1'(t_{2g}) \rightarrow a_2''(t_{2g})$ σ–σ^* excitation, determined in ref 34 by analysis of VT-absorption and resonance Raman spectroscopic data and Xα-SW calculations.

Particularly useful to this end is the observation of large resonance Raman enhancement of ^{18}O-sensitive $[Fe_2(OH)_3]^{2+}$ vibrations with $a_1'(t_{2g}) \rightarrow a_2''(t_{2g})$ excitation, as these directly probe the changes in bonding accompanying this excitation. Using RR vibrational intensities and VT-absorption bandshapes as experimental probes, the geometric distortions induced by the $a_1'(t_{2g}) \rightarrow a_2''(t_{2g})$ excitation in $[Fe_2(OH)_3(tmtacn)_2]^{2+}$ have been quantitatively analyzed, providing a set of excited-state parameters that uniquely satisfies the complementary requirements of these excited-state experiments. The results of this analysis (see ref 34) are included in Table 1 (right column and bottom). Figure 8 depicts the $[Fe_2(OH)_3]^{2+}$ excited-state distortion in terms of atomic displacements relative to the ground-state geometry and shows that the $a_1'(t_{2g}) \rightarrow a_2''(t_{2g})$ excited-state distortion primarily involves a significant increase in the metal–metal separation, consistent with the bonding description determined from the molecular orbital analyses (Figures 6 and 7) in which ~82–97% of the energy of this excitation is attributed to an Fe–Fe σ-bonding interaction. The geometry dependence of this splitting is estimated experimentally from the ground- and excited-state anharmonic potential surfaces used to simulate the $a_1'(t_{2g}) \rightarrow a_2''(t_{2g})$ VT-absorption and RR excitation profiles,[34] summarized schematically in Figure 9. The horizontal axis in Figure 9 represents the nuclear distortion coordinate shown in Figure 8, expressed in units of r_{Fe-Fe} (Å). As seen in Figure 9, the energy separation between ground- and excited-state potential surfaces differs between the distorted excited-state equilibrium geometry ($\Delta E_{2.89\ Å} = 10B_{ex} \approx 6850\ cm^{-1}$) and the ground-state equilibrium geometry ($\Delta E_{2.51\ Å} = 10B_{gr} = 13\,500\ cm^{-1}$). This observation allows estimation of the change in electronic coupling with change in Fe–Fe distance, providing a value of $\Delta B/\Delta r_{Fe-Fe} \approx 1750\ cm^{-1}$/Å.

Discussion

The above analyses allow definitive determination of the pathway for delocalization of the extra electron in this mixed-valence dimer. Both the molecular-orbital analyses and the nature of the $a_1'(t_{2g}) \rightarrow a_2''(t_{2g})$ excited-state distortion indicate that the ground state involves a significant direct σ-interaction between the d_{z^2} orbitals of the two Fe ions (Figures 6 and 7d), and it is this interaction that is responsible for valence delocalization and the observed ground-state properties. The magnitude of the double-exchange parameter, B, is therefore directly related to the overlap of these two d_{z^2} orbitals in $[Fe_2(OH)_3(tmtacn)_2]^{2+}$. This dimer is particularly well suited for direct metal–metal overlap due to its short (2.51 Å) Fe···Fe separation and trigonal site geometry, which places the extra electron in the $d_{z^2}(t_{2g})$ orbital oriented along the Fe···Fe internuclear axis. From the study of this complex, insight into the electronic structures of other mixed-valence dimers may also be gained.

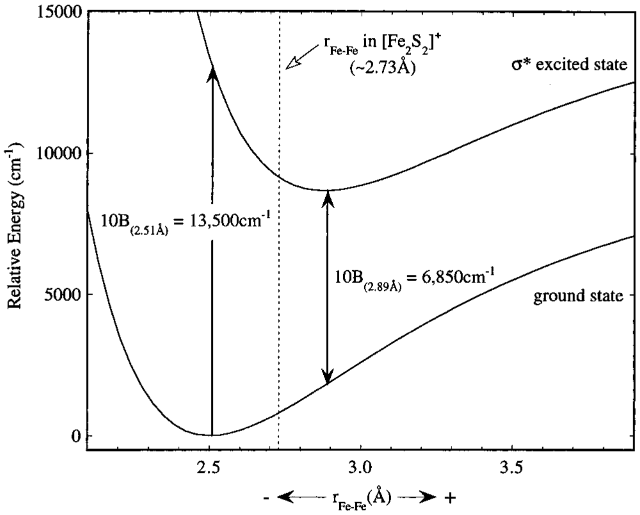

Figure 9. Effect of the excited-state nuclear distortion shown in Figure 8 on the double-exchange resonance splitting between $S = 9/2$ ground and σ^* excited spin-state components, indexed to the change in r_{Fe-Fe}. The dashed vertical line marks the value of r_{Fe-Fe} in $[Fe_2S_2]^+$ dimers.

The properties leading to valence delocalization in $[Fe_2(OH)_3(tmtacn)_2]^{2+}$ can be compared to those of two other classes of mixed-valence iron dimers, the $[Fe-(OH)-Fe]^{4+}$ active sites of half-met hemerythrin (Hr) and related non-heme coupled-diiron enzymes such as methane monooxygenase, the purple acid phosphatases, etc., and the $[Fe_2S_2]^+$ active sites found in “plant-type” ferredoxins and related iron–sulfur metalloenzymes. The two irons in half-met Hr and related dimers are bridged by a hydroxide group, occupy 6 (or 5 in the case of half-met Hr$_o$) coordinate sites, and are separated by ~3.4 Å.[6] The extra electron in these dimers occupies a $d_{xz,yz}(t_{2g})$ single-ion orbital (where z is defined by the Fe–OH bond) poorly oriented for direct metal–metal overlap. Since the Fe···Fe separation found in these and related dimers is too large for direct metal–metal overlap involving this d orbital, electronic coupling must instead be mediated by the bridging ligation. Mössbauer spectroscopy shows two distinct valences in these dimers,[6] and the observation of an IT transition in the absorption spectrum[57] indicates that the active sites are class II mixed-valence dimers. In the $[Fe_2S_2]^+$ dimer active sites, however, the iron d orbitals involved in valence delocalization are oriented favorably for direct overlap: the pseudotetrahedral geometries of the two iron sites in $[Fe_2S_2]^+$, separated by ~2.73 Å, place the extra electron in a d_{z^2} orbital directed along the Fe···Fe axis.[19,58a] Mössbauer spectroscopic studies of $[Fe_2S_2]^+$ ferredoxins show discreet Fe^{2+} and Fe^{3+} sites, however, and together with EPR spectroscopy further reveal that this dimer type has a valence-trapped $S = 1/2$ ground state involving antiferromagnetic coupling of the high-spin ferrous and ferric ions.[4,5] The valence-trapped $S = 1/2$ ground state is observed in high-symmetry $[Fe_2S_2]^+$ model complexes as well, indicating this configuration results not from the protein environment but from

---

[57] McCormick, J. M.; Reem, R. C.; Solomon, E. I. *J. Am. Chem. Soc.* **1991**, *113*, 9066–9079.

the properties of the iron−sulfur core itself.[58b] In higher-nuclearity iron−sulfur clusters valence delocalization is in fact observed,[4,5] suggesting that the structural and orbital prerequisites for delocalization in the two-iron ferredoxins exist but are outweighed by other contributions favoring localization.[59]

The very different ground-state properties of $[Fe_2(OH)_3(tmtacn)_2]^{2+}$ (delocalized $S = 9/2$) and $[Fe_2S_2]^+$ (localized $S = 1/2$) mixed-valence dimers despite their similar delocalization pathways warrants a more detailed comparison of these two systems. As described by eq 1, the ground-state magnetic properties of multiple-spin class III mixed-valence dimers can be described in terms of Heisenberg- and double-exchange contributions alone. In valence-trapped dimers such as $[Fe_2S_2]^+$, however, a complete ground-state description additionally requires consideration of vibronic-coupling effects. A comparison of the double-exchange, Heisenberg-exchange, and vibronic-coupling contributions to ground-state magnetism and valence delocalization in $[Fe_2(OH)_3(tmtacn)_2]^{2+}$ and $[Fe_2S_2]^+$ dimers is therefore presented below which provides an understanding of the striking differences between the ground states of these dimers.

Double-Exchange Contributions to Ground-State Magnetism. A prominent structural difference between these two dimers is the greater Fe$\cdots$Fe separation in $[Fe_2S_2]^+$ (~2.73 Å) than in $[Fe_2(OH)_3(tmtacn)_2]^{2+}$ (2.51 Å), as this will reduce the delocalization efficiency in the former by decreasing the d_{z^2}−d_{z^2} overlap. This difference can be estimated using the value of $\Delta B/\Delta r_{Fe-Fe} \approx 1750$ cm^{-1}/Å obtained from Figure 9 as described above. Although this value is determined by extrapolation and is likely subject to error due to nonlinearities in the relationship between B and r_{Fe-Fe}, and to the effects of specific ligation differences, the order of magnitude is expected to be reasonable since the energetics involved are dominated almost exclusively by d_{z^2}-d_{z^2} interactions (Figure 6). From this, the magnitude of B in $[Fe_2S_2]^+$ dimers ($r_{Fe-Fe} \approx 2.73$ Å, shown in Figure 9 as a dashed vertical line) is estimated to be ~965 cm^{-1}, or ~70% of that in $[Fe_2(OH)_3(tmtacn)_2]^{2+}$ ($B = 1350$ cm^{-1}). Thus, the greater metal−metal separation in $[Fe_2S_2]^+$ reduces the magnitude of B in this structure relative to $[Fe_2(OH)_3(tmtacn)_2]^{2+}$. Although reduced, B is still significant and must be overcome by a combination of Heisenberg antiferromagnetism and vibronic-trapping mechanisms in order to achieve the experimentally-observed localized $S = 1/2$ ground state.

Heisenberg-Exchange Contributions to Ground-State Magnetism. The Heisenberg contribution to the ground-state magnetism of $[Fe_2(OH)_3(tmtacn)_2]^{2+}$ has been determined from both high-temperature magnetic-susceptibility measurements ($J > \sim -70$ cm^{-1}, Figure 2, inset) and excited-state splitting energies (-23 cm^{-1} $\leq J \leq +2$ cm^{-1}, Figure 6a) to be small. Comparing the specific orbital interactions involved in the dominant pair of superexchange orbitals of $[Fe_2(OH)_3(tmtacn)_2]^{2+}$, namely $e'(e_g)$ and $e''(e_g)$, parts c and f of Figure 7 show that both molecular orbitals involve Fe−OH σ^*-interactions that could serve as efficient exchange pathways, but their similar energies indicate that these interactions are comparable in the two molecular orbitals and consequently their net contribution to antiferromagnetism is small. The Fe−OH interactions in these two molecular orbitals are comparable largely due to the protonation of the bridging ligands, which in addition to causing a general reduction in covalency of the oxygen bridging atoms also specifically reduces the $e'(e_g)$−$e''(e_g)$ splitting by decreasing the $e'(e_g)$ Fe−OH antibonding interaction as described by eq 8c when $x_H < 1$. This is shown in Scheme 1a, which presents the $e'(e_g)$ and $e''(e_g)$ molecular orbitals in the Fe−OH−Fe (xz) plane and illustrates the proton contribution to only the higher-energy $e'(e_g)$ orbital. This depiction can be directly related to the Xα-SW molecular-orbital contours shown in Figure 7c,f for the $e'(e_g)$ and $e''(e_g)$ orbitals in the same Fe−OH−Fe plane. As seen in Scheme 1a and Figure 7c,f, the Fe−OH−Fe angle of ~80° does not significantly favor Fe−OH interactions in either of these two molecular orbitals, as would be required to split this pair.

Scheme 1

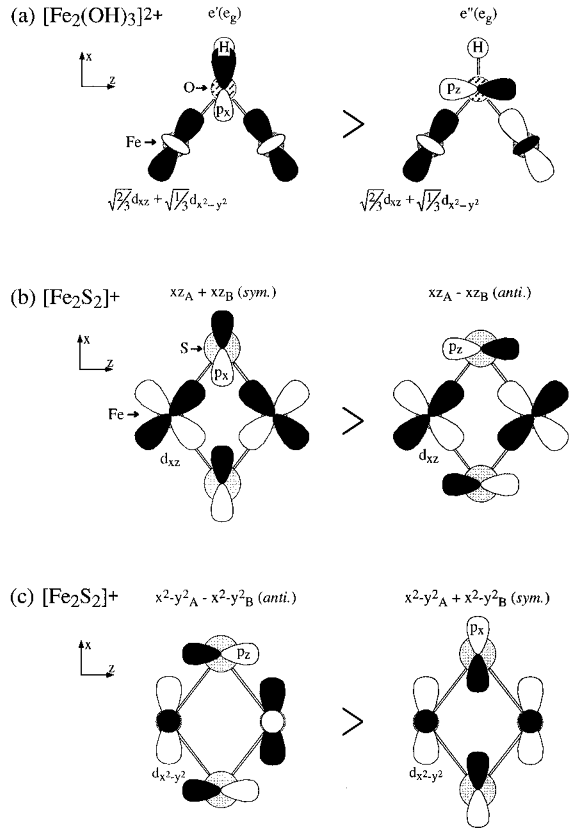

The superexchange contributions to the ground state of $[Fe_2(OH)_3(tmtacn)_2]^{2+}$ can be compared to those of the $[Fe_2S_2]^+$ ferredoxin active site. An experimental value of $J_{eff} \approx -105$ cm^{-1} has been reported for the $[Fe_2S_2]^+$ ferredoxin active site,[60,61] determined from the experimental splitting energy of $\Delta_{3/2-1/2} \approx 315$ cm^{-1} and the assumption of Heisenberg spin energetics (*i.e.*, $E(S) = -JS(S+1)$). From eq 1, the ratios of $|B/J|$ at which the ground-state spin changes are 9 ($9/2 \leftrightarrow 7/2$), 7 ($7/2 \leftrightarrow 5/2$), 5 ($5/2 \leftrightarrow 3/2$), and 3 ($3/2 \leftrightarrow 1/2$) for $J < 0$. When $|B/J| > 9$ the ground state is $S = 9/2$, while for $|B/J| < 3$ the ground state is $S = 1/2$. Using $J_{eff} \approx -105$ cm^{-1} and $B = 965$ cm^{-1} (estimated from the $\Delta B/\Delta r_{Fe-Fe}$ of $[Fe_2(OH)_3(tmtacn)_2]^{2+}$, *vide supra*), $|B/J_{eff}| \approx 9.3$ and the ground state is calculated to be in the region of spin-crossover between 9/2 and 7/2 spin states, in contrast with the experimentally observed

---

[58] (a) Dunham, W. R.; Bearden, A. J.; Salmeen, I. T.; Palmer, G.; Sands, R. H.; Orme-Johnson, W. H.; Beinert, H. *Biochim. Biophys. Acta* **1971**, *253*, 134−152. (b) Mascharak, P. K.; Papaefthymiou, G. C.; Frankel, R. B.; Holm, R. H. *J. Am. Chem. Soc.* **1981**, *103*, 6110−6116.

[59] Indeed, $S = 9/2$ ground-state magnetic properties have very recently been reported for two mutants of *C. pasteurianum* ferredoxin, and although Mössbauer studies are still needed to determine their degree of valence delocalization, this ferromagnetism is likely a manifestation of double exchange. Crouse, B. R.; Meyer, J.; Johnson, M. K. *J. Am. Chem. Soc.* **1995**, *117*, 9612−9613.

[60] Petersson, L.; Cammack, R.; Rao, K. K. *Biochim. Biophys. Acta* **1980**, *622*, 18−24.

[61] Palmer, G. In *Iron-Sulfur Proteins*; Lovenberg, W., Ed.; Academic Press: New York, 1973; pp 285−325.

$S = 1/2$ ground state in these systems. This disagreement results from the initial assumption of Heisenberg spin energetics (*i.e.*, the use of J_{eff} to represent the true Heisenberg-exchange parameter, J) which is only valid when $B = 0$. If $B \neq 0$, the observed splitting between ground and first-excited spin states ($-3J_{\mathrm{eff}} = \Delta_{3/2-1/2}$) is described by eq 1 as $\Delta_{3/2-1/2} = -3J - B$, which yields $J \approx -430$ cm^{-1} (for $B = 965$ cm^{-1} and $\Delta_{3/2-1/2} = 315$ cm^{-1}). Thus, the reported J_{eff} value derived under the assumption of pure Heisenberg spin energetics represents a lower limit for the true magnitude of J, and taking double exchange into account in the analysis of J reveals that superexchange antiferromagnetism in $[\mathrm{Fe_2S_2}]^+$ dimers ($J \approx -430$ cm^{-1}) is significantly greater than in $[\mathrm{Fe_2(OH)_3(tmtacn)_2}]^{2+}$ ($J > -70$ cm^{-1}). Note that eq 1 is only valid for *delocalized* spin states, and since the $S = 1/2$ ground states of $[\mathrm{Fe_2S_2}]^+$ dimers are known experimentally to be valence *localized*, valence-trapping effects must also be considered in order to obtain an accurate J value (*vide infra*).

The large differences in Heisenberg exchange-coupling values, J, between $[\mathrm{Fe_2(OH)_3(tmtacn)_2}]^{2+}$ and $[\mathrm{Fe_2S_2}]^+$ dimers can be related to differences in superexchange orbital pathways and bridging-ligand covalency. The dominant contributions to superexchange in $[\mathrm{Fe_2S_2}]^+$ dimers are made by splittings of the $(xz)_{\mathrm{s,a}}$ and $(x^2 - y^2)_{\mathrm{s,a}}$ pairs, with other interactions making smaller but significant contributions.[15,62,63] The molecular orbitals that dominate superexchange in $[\mathrm{Fe_2S_2}]^+$ dimers are illustrated in Scheme 1b,c. The $[\mathrm{Fe_2S_2}]^+$ superexchange orbital interactions shown in Scheme 1b are similar to those of $[\mathrm{Fe_2(OH)_3(tmtacn)_2}]^{2+}$ shown in Scheme 1a, but contribute more to the ground-state antiferromagnetism due to the greater covalency of the S^{2-} bridges in $[\mathrm{Fe_2S_2}]^+$ relative to the protonated OH^- bridges of $[\mathrm{Fe_2(OH)_3(tmtacn)_2}]^{2+}$, and to the smaller bridging angle (~75° *vs* 80° in $[\mathrm{Fe_2(OH)_3(tmtacn)_2}]^{2+}$). In addition, the superexchange orbital interactions shown in Scheme 1c, which involve overlap of the iron $\mathrm{d}_{x^2-y^2}$ orbitals with the sulfur p_x and p_z bridging orbitals, also contribute significantly to J in $[\mathrm{Fe_2S_2}]^+$ dimers,[15,62,63] whereas the analogous orbital pair in $[\mathrm{Fe_2(OH)_3(tmtacn)_2}]^{2+}$ ($\mathrm{e}'(\mathrm{t_{2g}}) - \mathrm{e}''(\mathrm{t_{2g}})$, Figure 7b,e) is relatively ineffective.

In summary, Heisenberg-exchange coupling in the iron–sulfur dimers is substantially more antiferromagnetic than that in $[\mathrm{Fe_2(OH)_3(tmtacn)_2}]^{2+}$ (-430 cm^{-1} *vs* > -70 cm^{-1}), and this is attributable to differences in bridging-ligand covalency and the specific effects of bridge protonation on metal–ligand orbital overlap. Since $\Delta_{S,S\pm1}$ is more sensitive to changes in J than in B (for example, $\Delta_{7/2-9/2}$ is constant for a constant value of $B + 9J$, from eq 1), this difference in J is far more significant than the ~30% reduction of B in $[\mathrm{Fe_2S_2}]^+$ dimers in determining the different ground-state electronic properties of the $[\mathrm{Fe_2S_2}]^+$ and $[\mathrm{Fe_2(OH)_3(tmtacn)_2}]^{2+}$ systems.

Vibronic Contributions to Valence-Trapping and Ground-State Properties. In addition to B and J, static and/or dynamic symmetry-breaking mechanisms also contribute to the ground-state properties of these mixed-valence dimers. While $[\mathrm{Fe_2S_2}]^+$ sites in proteins may have reduced symmetries imposed by the static protein environment, high-symmetry iron–sulfur models having no static symmetry-breaking environment still show trapped valences,[58] and hence of these two symmetry-breaking mechanisms only vibronic coupling must be considered as being inherent to the $[\mathrm{Fe_2S_2}]^+$ core. This mechanism involves electron–nuclear coupling along the Q_- vibrational normal coordinate, describable as the out-of-phase combination of breathing motions on the two monomeric subunits of the dimer: $Q_- = (1/\sqrt{2})(Q_{\mathrm{A}} - Q_{\mathrm{B}})$. The effect of vibronic coupling on spin energetics is described by eq 11.[14,16] The

$$E^{\mathrm{s,a}}(S) = -JS(S+1) + \frac{1}{2}\left(\frac{\lambda^2}{k_-}\right)x_-{}^2 \pm \left[\frac{1}{2}\left(\frac{\lambda^2}{k_-}\right)^2 x_-{}^2 + B^2\left(S + \frac{1}{2}\right)^2\right]^{1/2} \tag{11}$$

vibronic-coupling parameter is defined as, λ (cm^{-1}/Å) $= k_-(\Delta Q_-) = k_-(\sqrt{n}(\Delta r))$, where Δr (Å) is the difference in metal–ligand bond lengths between oxidized and reduced monomeric subunits (approximated from literature values), n is the coordination number of each ion (6 in $[\mathrm{Fe_2(OH)_3(tmtacn)_2}]^{2+}$ and 4 in $[\mathrm{Fe_2S_2(SR)_4}]^{3-}$), x_- is the dimensionless coordinate associated with the Q_- vibrational normal coordinate ($Q_- = (\lambda/k_-)x_-$) having vibrational frequency υ_- (cm^{-1}), and $k_- = 4\pi^2c^2m\upsilon_-^2$ is the force constant for nuclear distortion along this coordinate (in units of cm^{-1}/Å^2).[64]

From eq 11, the propensity for valence trapping is related to the quantity $B(S + 1/2)/(\lambda^2/k_-)$. The vibronic-coupling term, λ^2/k_-, is estimated in $[\mathrm{Fe_2S_2}]^+$ dimers from known Raman $a_1(Q_-)$ vibrational frequencies of reduced ferredoxins and geometric parameters of ferric and ferrous mononuclear iron complexes to be $\lambda^2/k_- \approx 3660$ cm^{-1} (from $\Delta r = 0.1$ Å,[65−67] $\upsilon_- = 310$ cm^{-1},[68,69] $\mu = 32$ g/mol), compared to the value of $\lambda^2/k_- \approx 2590$ cm^{-1} estimated for $[\mathrm{Fe_2(OH)_3(tmtacn)_2}]^{2+}$ (from $\Delta r = 0.1$ Å,[65−67] $\upsilon_- = 306$ cm^{-1},[34] $\mu = 15.5$ g/mol (average of 3 N + 3 OH). These values result in a ratio of $[(\lambda^2/k_-)_{\mathrm{FeS}}]/[(\lambda^2/k_-)_{\mathrm{FeOH}}] \approx 3660$ cm^{-1}/2590 cm^{-1} ≈ 1.4. This comparison indicates greater vibronic-trapping energies in $[\mathrm{Fe_2S_2}]^+$ than in $[\mathrm{Fe_2(OH)_3(tmtacn)_2}]^{2+}$, associated with the larger metal–ligand force constants in the iron–sulfur dimer.

Using the above parameters for B, J, and λ^2/k_-, eq 11 predicts a valence-delocalized $S = 9/2$ ground state for $[\mathrm{Fe_2(OH)_3(tmtacn)_2}]^{2+}$ as observed (Figure 10a). Inclusion of vibronic coupling in the description of the $[\mathrm{Fe_2S_2}]^+$ ground-state properties allows a refined value of J to be determined from the experimental J_{eff} values of these dimers. Solving for the value of J in $[\mathrm{Fe_2S_2}]^+$ dimers from eq 11 using $B = 965$ cm^{-1}, $\lambda^2/k_- = 3660$ cm^{-1}, $J_{\mathrm{eff}} \approx -105$ cm^{-1}, and $\Delta_{3/2-1/2} = -3J_{\mathrm{eff}}$ yields $J \approx -360$ cm^{-1} and predicts the resulting $S = 1/2$ ground state to be valence trapped as observed experimentally (Figure 10b). Note that the spin state plays a large role in the effectiveness of vibronic coupling in valence trapping, as illustrated in Figure 10, since the ratio of double-exchange to vibronic contributions, $B(S + 1/2)/(\lambda^2/k_-)$, results in a factor of ~1:5 difference in the relative weighting of the vibronic-trapping parameter between the $S = 9/2$ and $S = 1/2$ states of the same dimer, respectively.[16]

Conclusion

The strong ferromagnetism observed in $[\mathrm{Fe_2(OH)_3(tmtacn)_2}]^{2+}$ is attributable to three factors: (i) the direct overlap of the metal orbitals involved in valence delocalization, aided by the short Fe···Fe separation and the trigonal orientation of the d_{z^2} orbitals along the Fe···Fe axis, (ii) the inefficient antiferromagnetic

---

[62] Norman, J. G., Jr.; Kalbacher, B. J.; Jackels, S. C. *J. Chem. Soc., Chem. Commun.* **1978**, 1027−1029.

[63] Summerville, R. H.; Hoffmann, R. *J. Am. Chem. Soc.* **1976**, *98*, 7240−7254.

[64] k_n/hc gives units of cm^{-1}/Å^2. $m = \mu/6.02 \times 10^{23}$ mol^{-1}.

[65] Lane, R. W.; Ibers, J. A.; Frankel, R. B.; Papaefthymiou, G. C.; Holm, R. H. *J. Am. Chem. Soc.* **1977**, *99*, 84−98.

[66] Hair, N. J.; Beattie, J. K. *Inorg. Chem.* **1977**, *16*, 245−250.

[67] Snyder, B. S.; Patterson, G. S.; Abrahamson, A. J.; Holm, R. H. *J. Am. Chem. Soc.* **1989**, *111*, 5214−5223.

[68] Han, S.; Czernuszewicz, R. S.; Kimura, T.; Adams, M. W. W.; Spiro, T. G. *J. Am. Chem. Soc.* **1989**, *111*, 3505−3511.

[69] Fu, W.; Drozdzewski, P. M.; Davies, M. D.; Sligar, S. G.; Johnson, M. K. *J. Biol. Chem.* **1992**, *267*, 15502−15510.

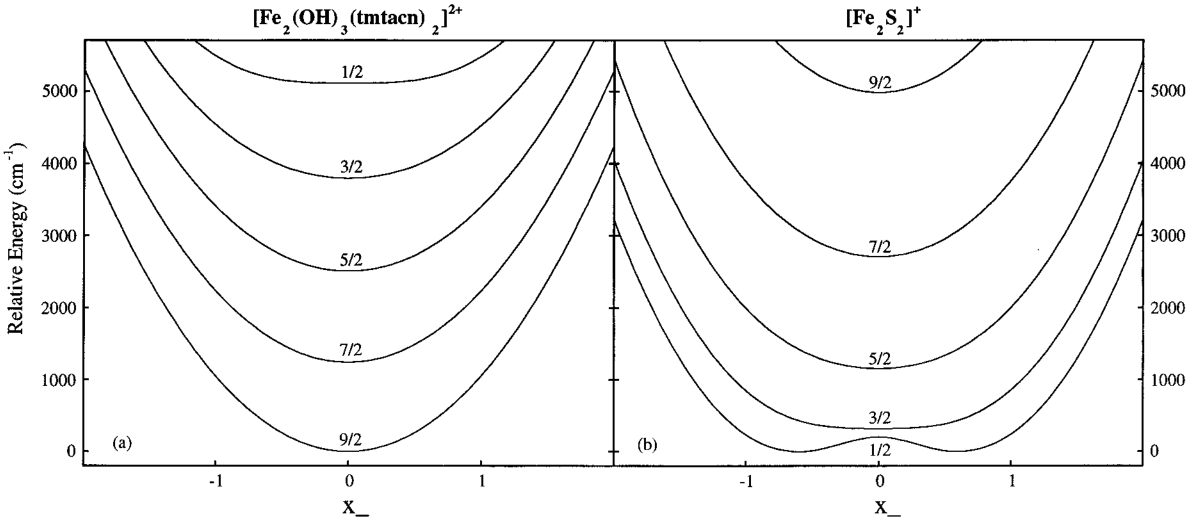

Figure 10. Ground and excited spin-state potential surfaces in the Q_- coordinate calculated from eq 11 and the parameters given in the text, showing (a) the delocalized $S = 9/2$ ground state of $[Fe_2(OH)_3(tmtacn)_2]^{2+}$ and (b) the localized $S = 1/2$ ground state of $[Fe_2S_2]^+$ dimers. The effect of S on valence delocalization is also apparent. The magnitude of $\Delta_{3/2-1/2}$ used in the discussion of (b) is taken as the difference between potential minima. Inclusion of zero-point vibrational energies in these potentials has minimal effect in (a) and requires an increase of ~25 cm^{-1} in the estimated value of J in (b) to maintain the condition $\Delta_{3/2-1/2} \approx 315$ cm^{-1}.

Table 3. Experimental Parameters Describing the Ground-State Magnetic and Valence-Delocalization Properties of $[Fe_2(OH)_3(tmtacn)_2]^{2+}$ and $[Fe_2S_2]^+$ Dimers

	$[Fe_2(OH)_3(tmtacn)_2]^{2+}$	$[Fe_2S_2]^+$	ratio $[Fe_2(OH)_3]^{2+}$:$[Fe_2S_2]^+$
B (cm^{-1})	1350	965	1.40
J (cm^{-1})	>-70	-360	<0.19
λ^2/k_- (cm^{-1})	2590	3660	0.71

superexchange interactions, poorly mediated by the protonated bridges, and to a lesser extent (iii) the small vibronic-trapping energetics, resulting from weak (*i.e.*, low force constant) Fe–OH bonds. The comparison of the parameters involved in ground-state magnetism and valence delocalization between $[Fe_2(OH)_3(tmtacn)_2]^{2+}$ and $[Fe_2S_2]^+$ systems is summarized in Table 3. On the basis of this comparison it is concluded that the valence-trapped $S = 1/2$ ground state observed in $[Fe_2S_2]^+$ dimers arises not as much from reduced double-exchange electronic coupling (B) as from the presence of good superexchange pathways for antiferromagnetic Heisenberg-exchange coupling that are able to overcome the effects of double exchange and lead to a low-spin dimer configuration, which is subsequently more susceptible to vibronic trapping. The efficient superexchange in $[Fe_2S_2]^+$ dimers is largely attributable to the highly-covalent sulfur bridging ligation, and this result further suggests that cluster formation to generate Fe_3S_4 and Fe_4S_4 units may significantly aid in valence delocalization of $[Fe_2S_2]^+$ pairs by impairing their superexchange pathways upon changing from μ_2- to μ_3-sulfur bridging ligation.[70]

Acknowledgment. The authors thank Professor W. S. Sheldrick (Ruhr-Universität Bochum) for the X-ray crystallographic data presented and L. B. LaCroix and D. E. Root for assistance with the Xα-SW calculations. E.I.S. thanks the NSF (Grants MCB9316768 and CHE9528250) for support of this research. E.L.B. gratefully acknowledges financial support by the National Institutes of Health (Grant GM22701) to Dr. E. Münck.

Supporting Information Available: Tables reporting X-ray crystallographic fractional coordinates, bond lengths and angles, anisotropic temperature factors, depictions of crystal morphology, and tables reporting input parameters for SCF-Xα-SW calculations (6 pages). See any current masthead page for ordering and Internet access instructions.

JA9536633

---

(70) **Note Added in Proof**: Very recent Mössbauer studies demonstrate that the $S = 9/2$ ground states observed in ref 59 are valence delocalized. Achim, C.; Golinelli, M. P.; Bominaar, E. L.; Meyer, J.; Münck, E. *J. Am. Chem. Soc.*, in press.